



1 **A 2700-year annual timescale and accumulation history for** 2 **an ice core from Roosevelt Island, West Antarctica**

3 Mai Winstrup¹, Paul Vallelonga¹, Helle A. Kjær¹, Tyler J. Fudge², James E. Lee³, Marie H.
4 Riis¹, Ross Edwards⁴, Nancy A.N. Bertler^{5,6}, Thomas Blunier¹, Ed J. Brook³, Christo Buizert³,
5 Gabriela Ciobanu¹, Howard Conway², Dorthe Dahl-Jensen¹, Aja Ellis⁴, B. Daniel
6 Emanuelsson^{5,6}, Elizabeth D. Keller⁶, Andrei Kurbatov⁷, Paul Mayewski⁷, Peter D. Neff⁸,
7 Rebecca Pyne⁶, Marius F. Simonsen¹, Anders Svensson¹, Andrea Tuohy^{5,6}, Ed Waddington²,
8 Sarah Wheatley⁷

9 1: Centre for Ice and Climate, Niels Bohr Institute, University of Copenhagen, Copenhagen,
10 Denmark

11 2: Earth and Space Sciences, University of Washington, Seattle, WA, USA

12 3: College of Earth, Ocean, and Atmospheric Sciences, Oregon State University, Corvallis,
13 OR, USA

14 4: Physics and Astronomy, Curtin University, Perth, Western Australia, Australia

15 5: Antarctic Research Centre, Victoria University Wellington, Wellington, New Zealand

16 6: GNS Science, Lower Hutt, New Zealand

17 7: Climate Change Institute, University of Maine, Orono, Maine, USA

18 8: Earth and Environmental Sciences, University of Rochester, Rochester, NY, USA

19 *Correspondance to: Mai Winstrup (mai@gfy.ku.dk)*

20 **Abstract**

21 We present a 2700-year annually resolved timescale for the Roosevelt Island Climate
22 Evolution (RICE) ice core, and reconstruct a snow accumulation history for the coastal sector
23 of the Ross Ice Shelf in West Antarctica. The timescale was constructed by identifying annual
24 layers in multiple ice-core impurity records, employing both manual and automated counting
25 approaches, and constitutes the top part of the Roosevelt Island Ice Core Chronology 2017
26 (RICE17). The maritime setting of Roosevelt Island results in high sulfate influx from sea
27 salts and marine biogenic emissions, which prohibits a routine detection of volcanic eruptions
28 in the ice-core records. This led to the use of non-traditional chronological techniques for
29 validating the timescale: RICE was synchronized to the WAIS Divide ice core, on the
30 WD2014 timescale, using volcanic attribution based on direct measurements of ice-core
31 acidity, as well as records of globally-synchronous, centennial-scale variability in atmospheric
32 methane concentrations.

33 The RICE accumulation history suggests stable values of 0.25 m water equivalent (w.e) per
34 year until around 1260 CE. Uncertainties in the correction for ice flow thinning of annual
35 layers with depth do not allow a firm conclusion about long-term trends in accumulation rates
36 during this early period but from 1260 CE to the present, accumulation rate trends have been
37 consistently negative. The decrease in accumulation rates has been increasingly rapid over the
38 last centuries, with the decrease since 1950 CE being more than 7 times greater than the
39 average over the last 300 years. The current accumulation rate of 0.22 ± 0.06 m w.e y^{-1}
40 (average since 1950 CE, $\pm 1\sigma$) is 1.49 standard deviations (86th percentile) below the mean of
41 50-year average accumulation rates observed over the last 2700 years.



1 Introduction

2 Accurate timescales are fundamental for reliable interpretation of paleoclimate archives. A
3 wide variety of dating methods are available for producing ice-core chronologies, with the
4 technique to be applied primarily depending on data availability. Data availability is
5 influenced by the analytical capabilities at the time of measurement as well as the limitations
6 specific to the ice-core site, with important site parameters including core quality,
7 accumulation rates, temperature, ice flow effects and surface snow remobilization.

8 Where annual snow deposition is sufficiently high and reasonably regular throughout the
9 year, seasonal variations in site temperature and atmospheric impurity deposition lead to
10 annual cycles in the ice-core water isotope and impurity records (Rasmussen et al., 2014). By
11 identifying and counting these annual cycles, a high-resolution annual-layer-counted ice-core
12 timescale can be produced (Sigl et al., 2016; Steig et al., 2005; Svensson et al., 2008; Taylor
13 et al., 2004). This technique is commonly employed for producing ice-core timescales at sites
14 with moderate to high snow accumulation, such as central Greenland, coastal Antarctica and
15 mountain glaciers, but has been demonstrated also for ice from Dome Fuji on the low-
16 accumulation East Antarctic Plateau (Svensson et al., 2015). Annual-layer-counted ice-core
17 timescales have traditionally been obtained by manual counting, but this task can now be
18 performed using machine-learning algorithms for pattern recognition (Winstrup et al., 2012).

19 Where possible, identification of annual layers allows the development of a high-resolution
20 ice-core chronology, but unless constrained by other data, the uncertainty of such timescale
21 will increase with depth, as the number of uncertain layers encountered accumulate to
22 produce some age uncertainty (Andersen et al., 2006; Rasmussen et al., 2007). Established
23 marker horizons found in the ice-core records can be used to evaluate the precision of a layer-
24 counted timescale, or, alternatively, to constrain the timescale. Such marker horizons include
25 layers of enhanced radioactivity resulting from nuclear bomb tests in the 1950s and 1960s
26 (Arienzo et al., 2016), sulfuric acids (Hammer, 1980) and/or tephra (Abbott et al., 2012) from
27 volcanic eruptions, and layers of enhanced flux of cosmogenic radionuclides resulting from
28 abrupt changes in the Earth's magnetic field (Raisbeck et al. 2007), short-lived cosmic events
29 (Sigl et al., 2015), as well as decadal variability in solar activity (Muscheler et al. 2014).
30 Given the global nature of many of these events, they form strata for synchronization across
31 ice cores and, in some cases, from ice cores to other climate archives such as tree-ring records
32 (Sigl et al. 2015) and lake and marine sediment cores (Davies et al., 2010).

33 Ice cores can also be stratigraphically matched using records of atmospheric composition of
34 trapped air. Mixing in the atmosphere causes variations in atmospheric composition of
35 relatively long-lived gases to be globally synchronous, and large-scale changes in gas
36 composition associated with abrupt climate events have been used as bi-polar ice-core
37 stratigraphic markers (Bender et al., 1994; Blunier et al., 1998; Blunier and Brook, 2001;
38 EPICA community members, 2006). Globally-synchronous multi-decadal fluctuations in
39 atmospheric composition also exist during periods of stable climate (Bender et al., 1994).
40 Recent improvements in measurement methods allow these to be measured far back in time
41 (Mitchell et al., 2013), whereby the ice-core gas records can be used for synchronizing ice
42 cores on sub-centennial timescales. During the snow densification process, there is a
43 continuous transfer of contemporary air down to the gas lock-in depth, resulting in an offset
44 between the ages of ice and gas at a given depth (Schwander and Stauffer, 1984). This age
45 difference, Δ_{age} , and how it changes with depth, can be calculated from firn densification
46 models (Herron and Langway, 1980), whereby the ice-core gas records also can be used to
47 synchronize ice-core records measured on the ice matrix (Buizert et al., 2015).



1 Annually-resolved ice-core chronologies provide long-term reconstructions of the annual
2 snowfall accumulation (Alley et al., 1993; Dahl-Jensen et al., 1993). Based on the ice-core
3 chronology, annual layer thicknesses at a given depth can be converted to past accumulation
4 rates by applying corrections due to density changes during the transformation from snow to
5 ice (Herron and Langway, 1980), and subsequent thinning of annual layers caused by ice flow
6 (Nye, 1963). Reconstructions of past snow accumulation on glaciers and ice sheets are
7 important for improving our understanding of natural fluctuations in regional accumulation
8 rates and their dependency on climate. This knowledge is essential to accurately evaluate the
9 current and future surface mass balance of glaciers and ice sheets, a critical and currently
10 under-constrained factor in sea level assessments (Shepherd et al., 2012).

11 Ice cores provide long-term absolute accumulation histories from a single location. They
12 thereby provide a context for other observations of past and current accumulation rates: Direct
13 surface observations allow detailed assessment of current spatial accumulation patterns
14 (Frezzotti et al., 2007) but do not inform about past variability, and internal layers of equal
15 age (isochrones) observed using ice-penetrating radar provide spatial coverage of past relative
16 accumulation patterns (Medley et al., 2013), but additional information is required for
17 converting these to absolute accumulation rates. Regional-scale reconstructions of past
18 surface mass balance can be obtained by coupling spatial information from climate models
19 and surface observations with point estimates of past accumulation rates derived from ice
20 cores (Frezzotti et al., 2013; Frieler et al., 2015). Within the PAGES network, the
21 Antarctica2k consortium seeks to produce Antarctica-wide reconstructions of temperature and
22 ice-core snow accumulation for the past 2000 years. The ice-core accumulation record
23 developed here is a contribution to the Antarctica2k network (Stenni et al., 2017; Thomas et
24 al., 2017) from an otherwise poorly-constrained sector of the Antarctic continent.

25 2. Site characteristics

26 From 2010 to 2014, the Roosevelt Island Climate Evolution (RICE) project extensively
27 sampled snow and ice at the summit of Roosevelt Island (Bertler et al., 2017). Roosevelt
28 Island is located within the eastern part of the Ross Ice Shelf (Fig. 1), from which it protrudes
29 as an ice dome that is grounded 200 m below sea level. The annual mean temperature derived
30 for Roosevelt Island from the ERA-Interim (ERAi) reanalysis data set of the European Centre
31 for Medium-Range Weather Forecasts (Dee et al., 2011) is $-27.4 \pm 2.4^\circ \text{C}$. An automated
32 weather station at the RICE camp measured the current accumulation rate to be 0.20 m w.e
33 yr^{-1} , consistent with previous estimates of $0.16\text{-}0.20 \text{ m w.e yr}^{-1}$ (Conway et al., 1999; Herron
34 and Langway, 1980). An array of 144 snow stakes monitored from 2010-2013 and covering a
35 200 km^2 region showed that snow accumulation across Roosevelt Island Dome ranged
36 spatially from $0.09\text{-}0.30 \text{ m w.e yr}^{-1}$ (Bertler et al., 2017). The drill site has an altitude of 550
37 m above sea level, and the ice thickness is 765 m.

38 The RICE project builds on preliminary site studies conducted in the 1970s and 90s. As part
39 of the US Ross Ice Shelf Project (RISP; 1973-1979) 95 firm cores were collected across the
40 Ross Ice Shelf, including two firm cores from Roosevelt Island summit, for evaluation of
41 present accumulation rates and its spatial variability over the region (Clausen et al., 1979).
42 The shortest (11 m) firm core from near the summit was measured for water isotopes and total
43 β -activity; here we refer to it as RID-75 (Table 1).

44 In 1997, ice-penetrating radar surveys across Roosevelt Island demonstrated extensive
45 internal layering which were assumed to be isochrones. Notably, the isochrones bend up
46 underneath the ice divide forming a so-called Raymond bump (Conway et al., 1999), a
47 glaciological feature indicative of stable ice divide flow over long (kyr) timescales (Raymond,



1 1983). Model reconstructions based on the shape and size of the Raymond bump suggest that
2 the current divide-type flow in the Roosevelt Island ice cap started between 2300 and 4200
3 years ago, with the best fit corresponding to onset of divide flow around 3000 years ago
4 (Martín et al., 2006). The stable flow regime since then facilitates the interpretation of past
5 accumulation rates from the annual layering in the RICE ice core. It has been hypothesized
6 that divide flow started as the grounding line in the Ross Sea Embayment moved south of
7 Roosevelt Island during the last deglaciation (Conway et al., 1999). Roosevelt Island is an
8 ideal location to investigate the timing of grounding-line retreat in the eastern Ross Sea, and
9 also to investigate changes in climate subsequent to the retreat of the grounding line.

10 The RICE ice cores were drilled at the present location of the Roosevelt Island ice divide
11 (Fig. 1), and less than 1 km from where the two RISP firn cores were drilled in 1974/75
12 (Clausen et al., 1979). The RICE deep core was drilled in austral summer 2011/12 and
13 2012/13. During the first season, the core was dry-drilled down to 130 m, and subsequently
14 extended during the second season using an Estisol-240/Coasol drilling fluid mixture.
15 Bedrock was reached at 764.6 m depth. The upper 344m of the core spans the last 2700 years;
16 the period for which an annual-layer counted timescale can be constructed. In addition to the
17 RICE deep core, several shallow cores were drilled in the vicinity. During the 2012/13 field
18 season, a 20m firn core (RICE-12/13-B) was drilled near the main core. This shallow core has
19 here been used here to preserve continuity of the ice-core records up to the 2012/13 snow
20 surface. A summary of the various relevant firn and ice cores collected at Roosevelt Island
21 summit is provided in Table 1.

22 In this paper, we first construct a layer-counted chronology for the RICE core, and validate it
23 against the WAIS Divide ice core WD2014 chronology (Sigl et al., 2015; Sigl et al., 2016).
24 We then use the annual layer thickness profile to reconstruct the accumulation history over
25 the last 2700 years, and consider the implications for mass balance in the Ross Ice Shelf
26 region. According to ERAi climate reanalysis data, precipitation rates at Roosevelt Island are
27 strongly influenced by the Amundsen Sea Low and associated ridging, and anti-correlated
28 with those in Ellsworth Land and the Antarctic Peninsula (Bertler et al., 2017; Emanuelsson
29 et al., 2017b; Yuan and Martinson, 2000). These differences illustrate the importance of high
30 spatial and temporal information about past accumulation when reconstructing regional mass
31 balance. With its coastal location and low altitude, Roosevelt Island represents a quite
32 different climatic setting than the inland, high-altitude Antarctic ice-core sites; we expect that
33 the RICE core is more representative of climate evolution in the coastal Victoria Land sector
34 of Antarctica, as defined by Thomas et al. (2017). As one of a very few ice cores within this
35 sector of Antarctica, the RICE accumulation history is particularly relevant for calculations of
36 changes in Antarctic mass balance over time.

37 **3. Methods**

38 **3.1. Ice core processing and Continuous Flow Analysis (CFA)**

39 The RICE ice cores were processed and analyzed at the GNS Science ice-core facility in
40 Lower Hutt, New Zealand. The cores were cut longitudinally to produce, among others, a
41 15x35 mm triangular piece for water isotope analysis and two 35x35 mm square sticks for
42 CFA (Fig. 2). The second CFA piece was for use in case the core quality of the primary piece
43 was compromised or for repeat measurements to test measurement accuracy and system
44 stability. The remaining core was used for measurements of gas composition, dust, tephra,
45 biology and physical properties, with a quarter of the ice core left as an archive piece.



1 In parallel with ice core cutting and processing, CFA and electrical conductivity
2 measurements (ECM) were carried out during measurement campaigns in 2012-2014 (Table
3 1). ECM was measured using a low-power hand-held ECM instrument (Icefield Instruments
4 Inc.) directly on the ice-core surfaces after the initial cutting of the ice core. In August 2012,
5 the uppermost section (8.57-40 m) of the RICE main core was processed and analyzed using
6 the GNS melter system, in which melt water was continuously collected into vials for
7 subsequent discrete analysis of various ion concentrations. In May 2013, this set-up was
8 replaced by an expanded version of the Copenhagen CFA system (Bigler et al., 2011),
9 providing high-resolution continuous measurements of liquid conductivity, calcium (Ca^{2+}),
10 insoluble dust particles, acidity (H^+), and black carbon (BC), as well as stable water isotopes
11 (δD , $\delta^{18}\text{O}$) and methane gas concentrations. Using this system, the RICE-12/13-B firn core
12 was analyzed. Next, the RICE main core was melted and analyzed from 40 m to 475 m, at this
13 depth the ice brittle zone was reached. Subsequently, repeat measurements of the top section
14 (8.57-40 m) of the main core were made using the second, parallel CFA stick. Ice from the
15 brittle zone, encountered from 475 m depth to bedrock, was allowed to relax for an additional
16 year before processing and CFA measurements. The last 2.6 m of the main core just above
17 bedrock (762 to 764.6 m) was reserved for analysis of DNA in entrained basal sediments.

18 Primary adaptations to the Copenhagen CFA system involved: 1) Depth assignment via a
19 digital decoder using 1 s time markers; 2) Inclusion of three fraction collectors for discrete
20 sample analyses by, respectively, ion chromatography (IC), Inductively-Coupled Plasma
21 Mass Spectrometry (ICP-MS), including measurements of ^{239}Pu using an ICP-SFMS
22 technique (Gabrieli et al., 2011), and a Los Gatos Research (LGR) water isotope analyzer
23 instrument; 3) Continuous analysis of stable water isotopes ($\delta^{18}\text{O}$, δD) using a LGR analyzer
24 (Emanuelsson et al., 2015); 4) Black carbon analysis by a Single Particle Soot Photometer
25 (Droplet Measurement Technologies, Boulder, CO; DMT SP2) using the method from
26 McConnell et al. (2007); 5) Acidity measurements using an optical dye method (Kjær et al.,
27 2016); and 6) Continuous methane concentration analysis using a Picarro Cavity Ring-Down
28 Spectroscopy (CRDS) instrument following the method reported by Stowasser et al. (2012).
29 Discrete samples of meltwater from the melthead outer section were collected for quality
30 assurance of the continuous stable water isotope measurements. See Figure 3 for a diagram of
31 the CFA system set-up.

32 The ice was melted at a rate of 3 cm min^{-1} , producing approximately 16.8 mL contamination-
33 free water and gas mixture per minute of melting. Air bubbles were separated in a debubbler
34 and sent to the Picarro CRDS instrument for methane analysis. Each minute, 5 mL meltwater
35 was directed to each of two fraction collectors (IC and ICP-MS aliquots) and 1.1 mL was
36 used for continuous measurements of water isotopes (0.05 mL) and black carbon (1.05 mL)
37 by the LGR and DMT SP2 instruments. The remaining 1.8 mL was sent to flow-through
38 liquid conductivity and insoluble particle analyzers (Bigler et al., 2011), and then split for
39 continuous analysis of soluble calcium (Traversi et al., 2007) and acidity (Kjær et al., 2016).
40 A third fraction collector was used to collect discrete samples for water isotopes from the
41 melthead overflow lines. On average, 20 meters of ice were melted during a 24-hour period,
42 including measurements, calibrations and routine maintenance. Calibrations for water
43 isotopes, calcium, acidity and black carbon was carried out before and after each melting run,
44 which consisted of the continuous analysis of 3x1m long ice rods. Calibrations for methane,
45 based on standard gases with methane concentrations corresponding to glacial and
46 preindustrial Holocene levels, were carried out twice daily.

47 The resulting CFA chemistry records are very densely sampled (1 data point per mm),
48 however mixing in the tubing as the meltwater sample travelled from melthead to the
49 analytical systems caused the true depth resolution of the system to be significantly less than



1 the sampling resolution. This was especially the case for the RICE CFA set-up due to the
2 relatively small fraction of total meltwater directed to the continuous measurement systems.
3 Following the technique used in Bigler et al. (2011), actual depth resolution for the CFA
4 measurements range from 0.8 cm (for conductivity) to 2.4 cm (for calcium) (see
5 supplementary Table S1).

6 **3.2. Constructing the Roosevelt Island Ice Core Chronology, RICE17, for** 7 **the last 2700 years**

8 The Roosevelt Island Ice Core Chronology 2017, RICE17, is constructed using multiple
9 approaches, as necessitated by changing properties and availability of data with depth. This
10 section describes the methodology used to construct the most recent 2700 years of the
11 RICE17 chronology, the period for which annual layer counting is feasible. For older sections
12 of the core, prior to the annual-layer counted interval, RICE17 is constructed by gas matching
13 to the WD2014 chronology for the WAIS Divide ice core, as reported in Lee et al. (2017).

14 **3.2.1. Overview of the annual-layer counting strategy**

15 For the uppermost section (0-42.5 m) of the RICE core, manual identification and counting of
16 annual layers was applied to records of water isotopes and ice impurities from the RICE main
17 core as well as the RICE-12/13B shallow core, where available. In this section, nuclear fall-
18 out and other distinctly identifiable marker horizons (Table 2, Sect. 3.2.3) in the ice-core
19 records were used to constrain the timescale. Below 42.5 m (1884 CE), development of the
20 timescale was augmented using the *StratiCounter* layer-counting algorithm (Winstrup et al.,
21 2012) using multiple CFA impurity records from the RICE main core. Unequivocal
22 identification of volcanoes in the RICE records was difficult, and consequently well
23 established volcanic marker horizons prior to 1884 CE (Sigl et al., 2015) were not used to
24 constrain the timescale. The only exception, in which an unequivocal volcanic event was
25 identified below 42.5 m depth, was a tephra layer at 165 m depth that is geochemically linked
26 to the Pleiades volcanic group. This tephra has been unequivocally identified in other West
27 Antarctic ice core records and dated to 1252±2 CE, and we used it to help constrain the
28 *StratiCounter* algorithm. Older than 1252 CE, RICE17 is a fully independent layer-counted
29 timescale. The chronology was validated by synchronization to the WAIS Divide WD2014
30 chronology by volcanic markers and methane matching.

31 The layer-counted part of RICE17 stops at 343.72 m (700 BCE). At this depth, the annual
32 layers are too thin (<6 cm) for reliable layer identification in data produced by the RICE CFA
33 set-up. Excellent agreement between the layer-counted timescale and the independent gas-
34 derived age at this depth allows us to produce the combined Roosevelt Island Ice Core
35 Chronology 2017, RICE17, by stitching the two together without any further adjustments.

36 **3.2.2. Manual layer counting with constraints (0 - 42.5 m; 2012 - 1884 CE)**

37 The top 42.5 m of the RICE17 chronology was obtained by manually counting annual layers
38 in the combined set of discretely-measured IC and ICP-MS data, where available, as well as
39 the continuous water isotope and chemistry records produced by the RICE CFA system. The
40 RICE main core starts at 8.57 m depth, so the top part of the timescale is based exclusively on
41 the RICE-12/13B shallow core. At 12.3 m, both cores display a distinct peak in their isotope
42 profiles, showing that they can be spliced directly without need for any depth adjustments.
43 Layer marks for the top 12.3 m were placed according to their depths in the RICE-12/13B
44 shallow core; below 12.3 m, layer marks are in reference to depth in the main core. In the
45 overlap section (8.57-19.41 m), we used the combined data set from both cores, thereby
46 reducing the risk of timescale errors caused by core breaks or bad data sections.



1 Layer counting in this section of the core relied predominantly on annual signals in non-sea-
2 salt sulfate (nss-SO_4^{2-}), acidity (H^+) and iodine, as these records displayed the most consistent
3 annual signals (Fig. 4). For the top 20 m, water isotope records contributed to annual layer
4 interpretations but smoothing through diffusion of water molecules in the firn causes the
5 annual signal to diminish with depth, such that annual layers were no longer visible below 20
6 m. Summers were identified as periods with high stable isotope ratios, high concentrations of
7 nss-SO_4^{2-} and associated acidity [originating from phytoplankton activity in the surrounding
8 ocean during summer (Legrand et al., 1991; Udisti et al., 1998)], and low iodine
9 concentrations [due to summertime photolysis of iodine in the snowpack (Frieß et al., 2010)].
10 Several other records also displayed annual variability, but much less reliably.

11 The detailed annual structure of the accumulation record derived from the layer counts
12 depends on the approach taken to place the layer marks. For this most recent period, layer
13 marks were placed as close as possible to the peak value in all data series with clear summer
14 peaks (isotope, sulfur/sulfate, acidity). The summer peaks are assigned to the beginning of the
15 calendar year (January 1st) as supported by ERAi near-surface air temperature and Amundsen
16 Sea Low (ASL) 500-hPa geopotential height (Emanuelsson et al., 2017b).

17 A confidence interval was assigned to the timescale by classifying layers as certain or
18 uncertain. Some uncertain layers were counted as a layer in the timescale, while others were
19 not, with the upper/lower bound of the age confidence interval being increased corresponding
20 to this choice. Classification of certain and uncertain layers in the timescale was achieved
21 while accounting for constraints imposed by timescale tie points (section 3.2.3). We constrain
22 the timescale to fit these age constraints, but conservatively estimate the uncertainty of the tie-
23 point ages to be ± 1 yr, thereby allowing for small uncertainties in e.g. precise deposition time
24 of volcanic material in the ice-core record. In this way, a most likely timescale was
25 constructed along with an uncertainty estimate, which we interpret as the 95% confidence
26 interval of the age at a given depth, similar to that obtained from automated counting deeper
27 in the core (see section 3.2.4). Figure 4 demonstrates the approach used to select certain and
28 uncertain annual layers in the RICE core records.

29 **3.2.3. Age constraints and timescale validation (0 - 42.5 m; 2012 - 1884 CE)**

30 **3.2.3.1 The 1974/75 snow surface**

31 The upper 42.5 m of the RICE17 chronology was tied to several unambiguous marker
32 horizons found in the ice-core records. The uppermost tie-point was established by
33 successfully matching the top of the previously-drilled RID-75 firn core with the RICE main
34 core by comparison of their respective water isotope profiles (Fig. 5). The first tie-point in the
35 RICE17 chronology is January 1975, at a depth of 14.62 m which corresponds to the snow
36 surface in the RID-75 firn core (Table 2).

37 **3.2.3.2 Nuclear bomb peaks**

38 The RID-75 core was previously annually dated using the water isotope profile along with
39 constraints from peaks in total specific β -activity from atmospheric nuclear bomb tests in the
40 mid-1950s and 1960s (Clausen et al., 1979). Isotope matching of the two cores is consistent
41 with high-resolution ^{239}Pu measurements on the RICE main core (Fig. 5).

42 Fallout from atmospheric nuclear bomb testing causes a significant increase in plutonium
43 levels (Table 2), starting from very low background levels at 22 m and reaching peak values
44 at 21.6 m in the RICE main core. This peak can be attributed to the Castle Bravo Operation,
45 when the US military detonated a very large hydrogen bomb at Bikini Atoll, Marshall Islands.
46 The operation took place in March 1954 and caused unexpectedly large amounts of nuclear
47 fall-out globally during the following year (see e.g. Arienzo et al. (2016)). The abrupt increase



1 in ^{239}Pu -fallout makes this horizon a reliable age marker, and it was used as an age constraint
2 during development of the RICE17 timescale.

3 Several subsequent peaks in the ^{239}Pu and β -activity records can be attributed to successive
4 nuclear tests and subsequent test ban treaties (Table 2). However, these peaks are broader and
5 less distinct, and hence were only used for timescale validation. Devastating effects of the
6 Castle Bravo operation led to a moratorium agreement between Britain, USA, and the Soviet
7 Union banning atmospheric nuclear testing, in effect by November 1958. The effect is slowly
8 decreasing values of ^{239}Pu in the RICE core, reaching minimum values in the early 1960s.
9 Following an uptake of Soviet atmospheric nuclear testing in 1961-62, the ^{239}Pu values
10 increased in 1962 (19.8 m), and increased levels of β -activity and ^{239}Pu concentrations
11 continued until 1966/67. A second broad peak starts summer 1970/71. This period of
12 enhanced radioactivity has been attributed to French bomb tests at Mururoa (21°S, 137°W)
13 taking place from 1969-1971 (Clausen et al., 1979); the 1971 peak in ^{239}Pu is the last episode
14 of enhanced ^{239}Pu levels in the RICE core.

15 3.2.3.3 Recent volcanic eruptions

16 Clearly-identifiable volcanic horizons formed the basis for establishing the recent part of the
17 RICE17 chronology. A tephra layer located at 18.1-18.2 m has a geochemical composition
18 similar to tephra from Raoul Island, New Zealand, which erupted from November 1964 to
19 April 1965 (Table 2). Tephra of similar composition has also been found in the WAIS Divide
20 core corresponding to late 1964. This tephra layer is located in early 1965 CE according to the
21 RICE17 chronology. Additionally, sulfate deposition from the eruptions of Santa Maria (1902
22 CE, RICE depth 37.45 m) and Krakatau (1883 CE, RICE depth 42.34 m) were used to
23 constrain the lower part of the manually-counted timescale, with ages in accordance with
24 WD2014.

25 We were unable to confidently pinpoint acid deposition from several other large volcanic
26 eruptions during recent times. This was the case for e.g. the Pinatubo eruption (1991 CE),
27 although a small peak in the conductivity and acidity profiles does fit the WD2014 age of
28 acidic fallout from this eruption. Similarly, we find potential volcanic acid deposition in the
29 1963 CE stratum, which may be affiliated with the Agung eruption (1963 CE).

30 Manual layer counting stopped at 42.3 m depth, where an acidic horizon indicates significant
31 sulfate deposition from the Krakatau eruption, Indonesia (August 1883 CE). According to the
32 WD2014 chronology, the sulfate horizon corresponding to this eruption was deposited
33 starting early 1884 CE, and continuing for several years thereafter. Accordingly, an age of
34 1884 CE was attributed to this horizon. This strata was used as starting point for the
35 automated counting routine, which generated the remaining part of the annual-layer counted
36 RICE17 timescale.

37 3.2.4. Automated annual layer counting (42.5 - 343.7m; 1884 CE – 700 BCE)

38 For the section 42.5-343.7 m (1884 CE – 700 BCE), the RICE17 annual layer-counted
39 timescale was established using the *StratiCounter* algorithm (Winstrup et al., 2012), extended
40 to interpret the annual signal based on multiple chemistry series in parallel (Winstrup, 2016).
41 *StratiCounter* is a Bayesian technique built on machine-learning methods for pattern
42 recognition, and it uses a Hidden Markov Model (HMM) framework (Rabiner, 1989).
43 *StratiCounter* infers the most likely timescale by counting annual layers in overlapping
44 batches of data stepwise down the ice core, with the length of each batch corresponding
45 approximately to a 50-year section. For each batch, the most likely annual layering is
46 calculated by combining *a priori* information on layer appearance – initially based on a small
47 section of the data used as a “training set” – with the observed annually-resolved data series.



1 *StratiCounter* works in an iterative manner, updating the *a priori* information (the annual
2 layer parameters) with each iteration until convergence is reached using optimal layering
3 parameters. The algorithm then proceeds to the next 50-year section of data. In this way, the
4 annual layers are allowed to slightly change characteristics with depth, as the layer
5 thicknesses decrease and the annual signals become smoother. Finally, a second source of
6 prior information (a set of generalized annual layer templates, which carries information on
7 e.g. relative peak phasing) is updated based on the retrieved layering, and *StratiCounter*
8 re-evaluates the entire timescale using this new set of templates (Winstrup, 2016). The output of
9 *StratiCounter* is a probability distribution of the age as function of depth, based on which the
10 most likely age can be estimated, as well as a 95% confidence bound on the age estimate. The
11 confidence interval assumes the timescale errors to be non-biased, so that uncertainties in
12 layer assignment partly cancel out over longer distances, giving rise to a non-linear increase
13 in uncertainty with depth.

14 For this deeper part of the RICE core, annual cycles were most reliably observed in the high-
15 resolution CFA measurements of black carbon (BC). The *StratiCounter* algorithm was
16 therefore tuned to select peaks in black carbon as the annual marker, while noting that it
17 generally peaks a little earlier in the year than the water isotope and acidity signals (see
18 Supplementary section S4), taken to indicate January 1st. Other CFA records also displayed
19 annual variations, particularly the acidity measurement, but tended to be less consistent. From
20 0 to 129 m, an annual signal was observed in the insoluble dust record (determined by laser
21 scattering) but the data below 129 m were corrupted by the presence of drill fluid in the CFA
22 system. Calcium and conductivity measurements sometimes displayed annual variations, but
23 were limited in their contribution to annual layer interpretations because multiple peaks per
24 year were frequently observed in these signals. The discretely-sampled ICP-MS data records
25 did not have sufficient resolution to resolve annual layers. *StratiCounter* was run based on the
26 full suite of CFA records: black carbon, acidity, dust, calcium, and conductivity, except that
27 the dust record was excluded in the contaminated lower part.

28 Due to the relatively shallow ice depth, layer thicknesses rapidly decrease with depth in the
29 Roosevelt Island ice core, thus it was necessary to make slight changes to the *StratiCounter*
30 algorithm settings through the depth range considered. We hence divided the ice-core records
31 into four sections, with section delimitations selected to span a given range of layer
32 thicknesses, as based on estimates obtained from methane matching to WAIS Divide (section
33 3.3.2). The algorithm was initialized based on an initial set of manual layer counts produced
34 for the interval 40-150 m. The *StratiCounter* procedure is described in more detail in
35 supplementary section S2. For the uppermost section, performance of the algorithm was
36 tested using a variety of smaller changes in algorithm settings, which all resulted in very
37 similar timescales (± 10 years at 165 m). The final settings were chosen as those for which the
38 timescale was in best agreement with the WD2014 age of a tephra layer located at 165 m
39 depth (see Section 3.3.1). This tephra has a geochemistry consistent with an eruption of the
40 Pleiades, West Antarctica (Kurbatov et al., 2015), and tephra of similar geochemistry has
41 been found in the WAIS Divide core with a corresponding age of 1252 ± 2 CE. This is
42 presently the only certain marker horizon in the RICE core below 42.5 m with a precise age
43 estimate, and the only horizon used to constrain the deeper part of the layer-counted section of
44 the RICE17 timescale. Proceeding to the deeper sections, the algorithm settings were kept as
45 similar as possible to those used in this upper part (Table S2).



1 **3.3. Validation of the RICE17 chronology**

2 The layer-counted RICE17 chronology was validated by 1) volcanic matching to WAIS
3 Divide on the WD2014 timescale, and 2) by matching multi-decadal variations in the RICE
4 methane record to a similar record from WAIS Divide.

5 Volcanic synchronization offers more precise validation between the age scales of the two
6 cores but suffers the risk of possible event misattribution. Distinct volcanic marker horizons
7 observed in the ice matrix are attributed in both cores, thereby offering very precise relative
8 and absolute age constraints. However, there is a risk that some of the volcanic match-points
9 are incorrectly identified. This risk is always present with volcanic matching, but here, the
10 risk is greater than usual since volcanic matching of RICE to other Antarctic ice cores was not
11 trivial. The extreme maritime environment of Roosevelt Island overwhelms the volcanic
12 signatures due to marine biogenic sulfate emissions, and traditional approaches failed for
13 reliable volcanic detection in the ice-core record. Adding to the challenge, many active
14 volcanoes exist in the vicinity of Roosevelt Island. Regional eruptions produce some of the
15 most discernable volcanic acidity peaks in the RICE ice-core records, and these complicate
16 the task of identifying large tropical eruptions useful for synchronizing to other Antarctic ice
17 cores. For more reliable identification of volcanic peaks in the RICE core, we use two new
18 volcanic proxies as described in section 3.3.1.1.

19 Methane gas synchronization points are less likely to be misattributed but do not allow for a
20 similarly precise matching due to the multi-decadal nature of methane variations as recorded
21 in the ice cores, and given the need to account for the gas-age-ice-age difference (Δ age).
22 Methane matching is thus less valuable for resolving small-scale and relative age uncertainties
23 of the layer-counted timescale. Absolute age control on the gas synchronization, however, is
24 better than that of volcanic matching. We can therefore use methane gas synchronization to
25 validate the absolute ages of the timescale and the volcanic match points.

26 Combining the two lines of evidence thus allows us to validate the RICE17 timescale with
27 high precision (from volcanic matching based on new volcanic tracers) as well as high
28 absolute age accuracy (from methane matching) (Fig. 6). Using the annual-layer counted
29 timescale as base for comparison, we successfully established a robust series of volcanic
30 match points between RICE and the WAIS Divide core (Table 2), which were subsequently
31 confirmed by methane matching of the two cores.

32 **3.3.1. Timescale validation by volcanic matching**

33 **3.3.1.1 Detection of volcanic eruptions using new proxies**

34 The low altitude and coastal location of the RICE ice-core site results in a large seasonal
35 influx of sulfate with biogenic emissions from the surrounding ocean, tending to obscure most
36 of the sulfur contributed by volcanic eruptions. The seasonal signal varies from almost no
37 sulfate during winter to summer peak values of up to 200 ppb non-sea-salt sulfate. For
38 comparison, in the WAIS Divide core, with accumulation rates of similar magnitude, sulfur
39 deposition from the large Tambora eruption (Indonesia, 1815 CE) gives rise to maximum
40 non-sea-salt sulfur concentrations of 80 ppb (Sigl et al., 2015). Consequently, in order to
41 observe volcanic signatures in the RICE core, very high-resolution records are required to
42 disentangle the sporadic influx of volcanic sulfur from the annual variability. Below 40 m, the
43 resolution of the discretely-sampled S record is too low (9.5 cm) for this purpose.

44 The RICE ice core acidity has been employed as a tracer of volcanic eruptions, rather than the
45 traditional approach of evaluating total sulfur content. In the atmosphere, volcanic emissions
46 of gaseous SO_2 are rapidly oxidized to H_2SO_4 , a strong acid. Only a fraction of biogenic



1 sulfur emissions, however, are oxidized to H_2SO_4 . Consequently, the relative magnitude of
2 volcanic versus biogenic influx is expected to be more significant in terms of acidity than
3 sulfur concentrations. This is especially the case for regional volcanic eruptions. The
4 prevalence of quiescent regional volcanism with relatively high halogen content in West
5 Antarctica (Zreda-Gostynka et al., 1997) implies that these halogens may contribute strongly
6 to the measured ice acidity. This is not the case for larger and more distant volcanoes, since
7 halogens are relatively quickly removed from the atmosphere during transport. Regional
8 eruptions will therefore generally have the clearest expression in the acidity records, which
9 causes additional challenges in volcanic synchronization of RICE to other ice cores.

10 Acids increase the conductivity of the ice, and two commonly used tracers for volcanic
11 activity are measurements of liquid conductivity and ECM. ECM measures the solid ice
12 conductivity, which is determined by the H^+ content in the ice, hence providing a direct
13 measure for acidity. Measurements of ECM and liquid conductivity on the RICE ice-core
14 were both strongly influenced by the high sea salt concentrations found in the ice. As
15 previously noted by Kjær et al. (2016), the RICE conductivity record is almost identical to the
16 mostly sea-salt-derived RICE calcium record (Figs. 4 and 7), suggesting sea spray to be the
17 main source for peaks in liquid conductivity. The high influx of sea salts at Roosevelt Island
18 hampers a volcanic attribution directly from the RICE conductivity record. By comparing to
19 the sea-salt-derived calcium concentrations, however, we were able to extract a proxy for
20 non-sea-salt conductivity as the conductivity excess. Being a secondary product, this tracer is
21 prone to measurement errors, calibration and co-registration uncertainties, as well as affected
22 by the different smoothing of the records during measurements. Thus, only very distinct
23 signals in non-sea-salt conductivity were used for identification of volcanic eruptions, and
24 only when confirmed by other lines of evidence.

25 A second new tracer for volcanic eruptions was based on the high-resolution CFA acidity
26 record, which directly registers the concentration of H^+ ions in meltwater from the core. Also
27 this record is influenced by the annual variability in acidic influx from oceanic biogenic
28 emissions, a high peak in which potentially may be mistaken for the imprint from a small
29 volcanic eruption. Large eruptions with high acidic influx were, however, distinctly visible.
30 Figure 7a displays a sequence of volcanic signals in the RICE acidity and non-sea-salt
31 conductivity (conductivity-to-calcium residual) records. Substantial evidence for high acidity
32 influx was required in both volcanic tracers for the positive attribution of a volcanic horizon.

33 3.3.1.2 The Pleiades tephra horizon

34 A visible tephra layer deposited at 165.01-165.02 m has been geochemically attributed to the
35 Pleiades volcanic group (Kurbatov et al., 2006; Narcisi et al., 2001) in the Victoria Land
36 region of Antarctica (Fig. 1). This tephra has previously been found in the Talos Dome
37 (TALDICE) and Siple Dome ice cores (Dunbar et al., 2003). It was also matched to a
38 contemporary (1252 ± 2 CE) tephra horizon in the WAIS divide ice core (pers. comm. Nelia
39 Dunbar, 2014) on the WD2014 timescale, which allowed a firm synchronization of the two
40 cores at this depth. During development of RICE17, this horizon was used to select the
41 optimal version of the layer-counted timescale (see section 3.2.4), resulting in a RICE17 age
42 of 1252 ± 13 CE for this horizon.

43 3.3.1.3 Volcanic synchronization to WAIS Divide

44 With the Pleiades tephra horizon as chronostratigraphic marker, and using the RICE17 layer-
45 counted timescale as guideline, the sequence of volcanic horizons identified in RICE could be
46 linked to a volcanic record from the WAIS Divide ice core on the WD2014 chronology (Sigl
47 et al., 2015) (Fig. 7b). The frequency of volcanic synchronization markers was quite variable,
48 with unambiguous attribution of synchronization points only possible where a sequence of



1 relatively large volcanic eruptions could be identified in both records. Consequently, some
2 time periods suffer from sparse coverage of reliable volcanic links (e.g., 125-150 m, 215-250
3 m, 270-280 m, 335-340 m).

4 RICE17 volcanic eruption ages are given in Table 2. This table also includes the
5 corresponding eruption ages based on the WD2014 chronology, which has a maximum
6 uncertainty of ± 7 years over the last 2700 years (Sigl et al., 2016). To facilitate depth
7 designation, we used the peak of the volcanic signatures in both cores as depth-age validation
8 points for the annual-layer-counted RICE17 timescale.

9 We note that several large and well-known volcanoes, routinely found in Antarctic ice cores,
10 are difficult to locate in the RICE acidity and conductivity records. This has a variety of
11 reasons. Some large volcanoes were located in broken core sections removed before CFA
12 measurements (e.g. around Tambora, 1815 CE) or within sections of bad data quality due to
13 the introduction of air or drill liquid in the CFA system. For sections with no CFA data, a
14 tentative attribution of these large volcanoes was made based on the limited evidence from the
15 non-sea-salt sulfur and ECM records, where possible (Table 2). At other times, volcanic
16 matching was impossible due to ambiguity caused by several closely-spaced acidic peaks in
17 RICE, and/or due to insufficient data to discriminate volcanically-produced acids from the
18 high acidic background level.

19 All validation points were found to be in agreement with the RICE17 chronology within the
20 assigned confidence interval. In the absence of additional constraints, which may become
21 available in future, we refrain from constraining the RICE17 chronology to exactly fit the
22 marker horizons, and retain its nature as an independently layer-counted timescale.

23 3.3.2. Timescale validation using decadal variability in methane records

24 Given the challenges in volcanic synchronization, a second validation of the RICE17
25 chronology was performed by matching variations in RICE gas records to similar records
26 from the WAIS Divide ice core (Lee et al., 2017). Records of atmospheric methane (CH_4) and
27 isotopic composition of molecular oxygen ($\delta^{18}\text{O}_{\text{atm}}$) reflect global changes in atmospheric
28 composition (Ferretti et al., 2005; Mitchell et al., 2013; Mitchell et al., 2011; Severinghaus et
29 al., 2009). Over recent millennia, the period in focus here, atmospheric $\delta^{18}\text{O}_{\text{atm}}$ concentrations
30 have remained stable, whereas the methane record displays multi-decadal fluctuations.
31 Corresponding fluctuations are found in gas records from WAIS Divide (Wais Divide Project
32 Members, 2013, 2015). Matching up the methane records from the two cores provided an
33 evaluation of the absolute accuracy of the annual-layer-counted RICE17 chronology.

34 The gas records from RICE and WAIS Divide were synchronized using a Monte Carlo
35 technique adapted from (Huybers, 2002; Lee et al., 2017). Subsequent manual adjustment to
36 the match-points (average adjustment: 9 years, and all smaller than 23 years) in this top part
37 of the two cores provided a slightly improved fit between the records. Given the stability of
38 the $\delta^{18}\text{O}_{\text{atm}}$ record over the last millennia, the synchronization was solely constrained by the
39 observed variability in the methane records. Synchronization was based on discretely-
40 measured gas records due to significant data gaps in the high-resolution CFA methane record.
41 Average sample resolution of the RICE CH_4 and $\delta^{18}\text{O}_{\text{atm}}$ records is 26 years, which
42 contributes to the matching uncertainty.

43 Matching records of past atmospheric composition provides the ice-core gas-age, i.e. the age
44 of the gas at a given depth. By modelling the densification process, the gas-age-to-ice-age
45 difference (Δage) can be calculated, and this correction factor can be applied to the ice-core
46 gas-ages to obtain the relevant ice-core ice-ages at a given depth. We estimated Δage by
47 applying a dynamic Herron-Langway firn densification model (Herron and Langway, 1980)



1 following Buizert et al. (2015). The densification model is described in detail in Lee et al.
2 (2017), and will only briefly be described here: It is forced using a site temperature history
3 derived from the RICE stable water isotopes, and the firn column thickness is constrained
4 using the isotopic composition of molecular nitrogen ($\delta^{15}\text{N}$ of N_2), while assuming a
5 convective zone thickness of 2 m. Ice flow thinning are based upon the vertical velocity of
6 layers measured using phase-sensitive radio echo sounding (pRES) (Kingslake et al., 2014),
7 also used for deriving accumulation rates from the observed annual layer thicknesses in the
8 RICE core (section 3.4).

9 The relatively high accumulation rates at RICE, and the relatively warm surface temperatures,
10 give rise to small values of Δage compared to most other Antarctic sites. More importantly,
11 the uncertainties associated with these Δage corrections are small: Estimated 1σ -uncertainties
12 on the Δage corrections over the last 2700 years are in the order of 30 years. Hence the gas-
13 based age markers, tightly constrained by the observed multi-decadal variability in
14 atmospheric CH_4 , provide a chronology that is independent of the annual-layer counting.

15 **3.4. Accumulation reconstruction**

16 The accumulation rate history is inferred from depth profiles of the annual-layer thickness,
17 with corrections for densification of the firn and thinning of layers due to ice flow. Below we
18 develop an accumulation history at Roosevelt Island for the past 2700 years.

19 **3.4.1. Changes in density with depth**

20 Bag-mean densities were measured on the main RICE core for the interval 8-130 m, at which
21 depth ice densities were reached (Bertler et al., 2017; Lee et al., 2017). In steady state,
22 densification of the upper 8 m of the firn is parameterized using the initial snow density and
23 the surface temperature, and further densification to ice depends on the stress from the
24 overburden (Herron and Langway, 1980). With an initial density of 0.41 g cm^{-3} , a surface
25 temperature of -22°C , and an accumulation rate of $0.22 \text{ m w.e yr}^{-1}$ the modelled density
26 profile provides a good fit to the observed values (Fig. S1). The modelled densities for the
27 upper 8 m provide a smooth transition to the measured density profile, and this profile was
28 used to establish annual layer thicknesses. Note that the surface temperature derived from
29 ERAi ($-27.4 \pm 2.4^\circ \text{C}$) is significantly lower than that used in the model.

30 The observed density profile is well approximated using the Herron-Langway model,
31 although it is slightly skewed towards less dense values due to strain in the firn, suggesting
32 that effects of wind-remobilization or surface melt have been minimal.

33 **3.4.2. Thinning of annual layers due to ice flow**

34 An estimate of vertical strain from ice flow is needed to extract information about the
35 accumulation-rate history from the annual layer thickness profile. Kingslake et al. (2014)
36 conducted repeat phase-sensitive radio-echo soundings (pRES) across Roosevelt Island to
37 measure the spatial pattern of modern vertical velocities. Near-surface vertical strain rates are
38 more compressive near the divide than on the flanks, which results in the distinctive stack of
39 Raymond arches visible in the radar-detected stratigraphy beneath the divide in Fig. 8b
40 (Raymond, 1983). Of particular interest is that the position of the modern divide is offset by
41 $\sim 500 \text{ m}$ from the peaks of the deeper arches, suggesting recent divide migration. Here we use
42 an approximation of the vertical velocity profile and constrain model parameters to (i)
43 account for changes in vertical velocity caused by divide migration; and (ii) match the
44 observed surface accumulation rate and estimate of ice sheet thinning.

45 The vertical velocity profile used here is found by fitting a model to measurements of
46 englacial vertical velocities [Fig. 8a, Kingslake et al. (2014)]. Following Kingslake et al.



1 (2014), we parameterize the vertical velocity profile at normalized height above the bed $w(\zeta)$
2 using a shape factor p and the vertical velocity at the surface w_s (Lliboutry, 1979):

$$w(\zeta) = w_s \left(1 - \frac{p+2}{p+1} \zeta + \frac{1}{p+1} \zeta^{p+2} \right)$$

3

4 Using $p=-1.22$ minimized the overall misfit to the measurements. Since no measurements
5 exist in the upper portion of the ice sheet (Fig. 8a), we choose to extend the velocity profile
6 linearly to the surface, starting at 155 m depth, in order to match w_s of 0.26 m i.e yr⁻¹. This
7 value of w_s was selected because it is the sum of the modern accumulation rate (0.24 m i.e yr⁻¹
8 over the past 50 years) and ice-sheet thinning for the past 2700 years (0.02 m i.e yr⁻¹). The
9 rate of ice-sheet thinning was estimated using an ice-flow model to match the dated
10 architecture of the Raymond stack (Fig. 8b).

11 The ice core was drilled on the modern divide but the Raymond arches at mid-depth are offset
12 by 500 m (Fig. 8b). The divide has likely migrated within the past several hundreds of years.
13 Observations from Roosevelt Island indicate the transition from divide- to flank-type flow at
14 Roosevelt Island occurs over distances of ~900 m (Kingslake et al., 2014). That is, ice
15 recovered in the ice core has experienced different vertical velocity regimes as the divide
16 position changed. Here we infer the evolution of the vertical velocity regime at the modern
17 divide using the architecture of the Raymond stack. For the core site, we construct a vertical
18 velocity profile appropriate for transitional-type flow between 344 m (700 BCE) until 1450
19 CE. We assume divide-flow after the divide reached its modern position 1450 CE. Figure 9
20 shows our inferred thinning function at the core site.

21 At the surface, uncertainty in the thinning function is zero (thinning has not started), but
22 uncertainties increase with depth. Uncertainty comes from: (i) the lack of pRES
23 measurements in the upper 90 m of the ice sheet to help constrain the near-surface vertical
24 velocity; and (ii) the vertical velocity profile may have varied over time in ways not
25 accounted for in this analysis. The second source of uncertainty is partly mitigated because
26 the Raymond Bump amplitude constrains the onset of divide flow to some time prior to 3000
27 yr ago (Martín et al., 2006). Hence most of the uncertainty in the thinning function for the
28 period of interest arises from the lack of measurements in the upper 90 m. To assess the
29 magnitude of the uncertainty we compare results using two alternate thinning functions. First,
30 we used the method described above to find the best fit when using a vertical surface velocity
31 of 0.24 m i.e yr⁻¹ (0.22 m w.e yr⁻¹), thereby neglecting the contribution from surface lowering.
32 Second, we used the best fit derived by Kingslake et al. (2014). The difference between the
33 thinning functions is a maximum at ~100 m depth. The mean difference between the thinning
34 functions was ~5%, with a maximum difference of 9%. Because other factors not accounted
35 for in this analysis may contribute additional uncertainty, we assume that the uncertainty
36 increases from zero at the surface, to 10% at 100 m depth (1630 CE), and then constant
37 uncertainty (10%) down to 344 m depth.

38

39 4. Results

40 4.1. The layer-counted RICE17 chronology

41 The RICE17 chronology covers the period back to 700 BCE (0-343.72 m), the past 2700
42 years. The majority of the timescale relies on CFA multi-parameter chemistry measurements,



1 with annual variations in black carbon as the most reliable annual tracer. Below 42.5 m (1884
2 CE), the timescale was produced using the *StratiCounter* annual-layer-counting algorithm,
3 fine-tuned to be in accordance with the WD2014 age of the Pleiades tephra layer at 165 m
4 depth - but otherwise it is an independent layer-counted timescale. This is also reflected in the
5 inferred confidence interval of the timescale, as the age uncertainty (± 13 years) at the Pleiades
6 tephra horizon is passed on to the deeper part of the timescale. Associated 95% confidence
7 intervals on the age-scale shows an approximately linear increase in age uncertainty with age,
8 corresponding to a faster-than-linear increase with depth (Fig. 6b). The uncertainty reaches a
9 maximum value of ± 45 years at 344 m, the end of the layer-counted section. The timescale
10 was validated by volcanic and gas synchronization to the WAIS Divide ice core on the
11 annually-layer counted WD2014 chronology (Sigl et al., 2015; Sigl et al., 2016), which has a
12 counting uncertainty of merely 7 years over the last 2700 years.

13 We observe that the layer-counted RICE17 timescale is consistent with the independent age
14 control points obtained by matching methane and atmospheric oxygen isotope ($\delta^{18}\text{O}_{\text{atm}}$)
15 records to WAIS Divide (Fig. 6b). Over the past 2700 years, there are 18 gas-age control
16 points. This results in an average spacing of 150 years, gradually increasing with depth.
17 Uncertainties in feature matching and calculation of Δage result in combined 2σ -uncertainties
18 for these control points of ~ 60 years. This uncertainty is primarily caused by synchronization
19 uncertainties (~ 48 years), and less so caused by uncertainties in Δage correction (~ 36 years).
20 Based on the automatic matching routine, agreement of RICE17 to the gas-matched ages is
21 better than 33 years for all control points, with a root-mean-square (RMS) difference between
22 the RICE17 and WD2014 timescales of 14 years. The average age difference is -1 years; as
23 the gas-age derived chronology and the annual layer counts are independent, the good
24 agreement indicates that there is no systematic bias in either the layer-counted chronology or
25 the methane age control points. Subsequent visual comparison of the two methane profiles
26 allowed slight manual adjustments to be made to the gas-age control points, which further
27 improved the matching. Using the modified age control points, agreement between WD2014
28 and RICE17 is better than 18 years with a RMS difference of 8.6 years.

29 Good agreement of the obtained volcanic marker horizons with both 1) absolute age markers
30 from methane matching, and 2) relative ages between volcanic markers as based on the
31 RICE17 chronology, strengthens our trust in the volcanic synchronization. Also from the
32 volcanic match points, we observe very good agreement between the RICE17 and WD2014
33 timescales. The agreement is especially remarkable down to 280 m (~ 200 CE), where the
34 observed discrepancies are less than ± 4 years at all marker horizons, with a RMS difference
35 of 14 years. This is much less than the inferred RICE17 age uncertainty at this depth (± 32
36 years), indicating that the inferred confidence bounds on the age-scale are reliable, albeit
37 somewhat conservative.

38 The decrease in layer thicknesses with depth causes the annual signal in the impurity records
39 to become increasingly difficult to reliably identify. At 280 m (200 CE), the depth resolution
40 of the CFA chemistry series (1-2 cm) is starting to become marginal compared to the annual
41 layer thicknesses (8 cm at 280 m depth). Nevertheless, the RICE17 chronology continues to
42 be in good accordance with the WD2014 timescale, although the volcanic matching indicates
43 that RICE17 has a slight bias ($\sim 2\%$) towards younger ages, meaning that some annual layers
44 are missed in the RICE records below 280 m. Consequently, the RICE17 chronology slowly
45 diverges from WD2014, reaching a maximum age difference of 30 years at the lowermost
46 volcanic age marker at 343.3 m (691.4 BCE, Table 2). This offset is within the derived
47 uncertainty on the timescale (45 years), and of similar magnitude as the uncertainty of the
48 methane-derived ages. As this age difference approaches the uncertainty of the methane-



1 derived RICE timescale developed in Lee et al. (2017), we decide to stop the layer-counts at
2 the gas-age control point at 344 m.

3 To extend the timescale for the RICE core further down, the high-resolution annual-layer
4 counted timescale is combined with the gas-matched timescale, which covers the entire core
5 with lower resolution. At the lowermost gas-age control point at 343.7 m, the two
6 independently derived RICE age-scales agree within 3 years. Hence, they can here be stitched
7 together directly without need for any further adjustments to form a continuous timescale for
8 the entire RICE ice core.

9 **4.2. Layer thicknesses**

10 RICE annual layer thicknesses decrease from more than 40 cm at the ice surface to ~6 cm at
11 344 m. Overall, the accuracy of the RICE17 timescale is supported by the smooth variations
12 of the annual layer thickness profile (Fig. 6a).

13 High inter-annual variability in RICE layer thicknesses adds to the challenge of correctly
14 identifying layers in the ice-core record. Annual layer thicknesses are distributed according to
15 a log-normal distribution with an average standard deviation of $\sigma = 0.28$. This implies that
16 1.3% of the layers will have a thickness that is either twice as large or less than half the most
17 common layer thickness. In the deeper part of the core, this corresponds to very thin layers
18 (<3 cm) that are unlikely to be resolved by any of the available records, likely contributing to
19 the small bias (~3%) towards undercounting of annual layers in the oldest part of the layer-
20 counted RICE17 timescale.

21 The high inter-annual variability in Roosevelt Island precipitation is likely caused by the
22 majority of the precipitation coming from individual storms bringing moisture to the location,
23 the number of which passing by Roosevelt Island may be highly variable from year to year. In
24 the top part of the RICE17 timescale, we observe 2010 CE to be a very thin layer,
25 corresponding to a year of very low accumulation (7.4 cm w.e). Hardly recognizable as an
26 annual layer from the ice core records themselves, this year has previously been identified as
27 an extremely dry and cold winter over large parts of Antarctica (Schlosser et al., 2016), and
28 ERA-interim data shows almost no accumulation at Roosevelt Island this year (Bertler et al.,
29 2017).

30 **4.3. Roosevelt Island accumulation history**

31 The RICE17 layer thicknesses were converted into past accumulation rates, by correcting for
32 density changes and ice flow thinning of annual layers with depth. The resulting accumulation
33 history over the last 2700 years is shown in Fig. 9, along with the uncertainty from ice flow
34 thinning when extending back in time.

35 **4.3.1. Spatial consistency in observed accumulation rates**

36 A very high degree of replicability in the derived year-to-year profile of layer thicknesses is
37 confirmed by comparing the accumulation rates obtained for the overlap sections of the three
38 available cores: RICE main core, RICE-12/13B, and RID-75. All cores were corrected for
39 density changes using the density profile from the RICE main core.

40 The three accumulation records are very strongly correlated (correlation coefficients ranging
41 between 0.85 and 0.87), indicating that the RICE annual layer thicknesses are representative
42 of local snow accumulation, and that depositional noise to a high degree can be disregarded
43 when converting annual layer thicknesses into estimates of past accumulation. The good
44 agreement between measured water isotope records from the cores (RICE main and RID-75,
45 Fig. 5) further confirms the consistency and stability of snow deposition at Roosevelt Island.



1 **4.3.2. Long-term accumulation trends**

2 From 700 BCE to around 1260 CE, the obtained RICE accumulation rates are slightly
3 increasing (Fig. 9), although the uncertainty from ice flow thinning prevents any definitive
4 conclusion on the trend during this period. At 1260 CE, the average accumulation rate reaches
5 $0.28 \text{ m w.e yr}^{-1}$, the maximum observed value over the last 2700 years. Since then, the
6 accumulation rate has decreased. An inflection point exists around 1700 CE, after which the
7 decrease in accumulation rates occurs more rapidly ($0.9 \text{ cm per century}$, Table 3). The current
8 accumulation rate, as averaged over the last 100 years, is $0.21 \text{ m w.e yr}^{-1}$, which is at the low
9 extreme of values observed in the record.

10 Uncertainties in the accumulation record arise from three factors: 1) the annual layer count, 2)
11 the measured density profile, and 3) the applied thinning function. The uncertainty on the
12 thinning function increases with depth and age (Fig. 9a; dotted lines). Except for in the
13 uppermost part of the record, uncertainties in the thinning function are by far the most
14 important, exceeding all other sources of uncertainty: At 500 BCE, close to the end of the
15 layer-counted section of RICE17, the possible range of accumulation rates spans from 0.17 m
16 w.e yr^{-1} . (i.e. significantly lower than today) to $0.4 \text{ m w.e yr}^{-1}$ (almost twice as large as today).
17 In our estimates for the 95% uncertainty bounds on past accumulation rates, we therefore
18 disregard the contribution from other sources than ice flow thinning of annual layers with
19 depth. However, we note that given the applied thinning function results in almost constant
20 accumulation levels in the earlier part of the RICE record, which may indicate that the
21 uncertainty of the thinning function is less than our conservative estimate of 10%.

22 The uncertainty in the thinning function implies a high uncertainty in inferring slow trends in
23 RICE accumulation rates over time, especially in the deeper part of the record. However, it
24 cannot explain the rapid decrease in accumulation observed in recent time.

25 **4.3.3. Large changes in recent accumulation rates**

26 For the most recent period, uncertainties associated with our derivation of accumulation rates
27 are small, and we can infer accumulation trends with greater confidence. This reveals a
28 distinct decrease in recent accumulation rates (Fig. 10). The decade from 1990-2000 CE was
29 the decade with the lowest accumulation rates since 1700 CE, and the most recent decade
30 from 2000-2010 CE also stands out as a decade with very low accumulation. Only two
31 previous decades (1850-1860 CE, 1950-1960 CE) have an average accumulation rate less
32 than those observed over the last two decades. The observed mean accumulation rate of the
33 last 10 years is $0.195 \text{ m w.e yr}^{-1}$, which is a 30% decrease in accumulation rates compared to
34 a 100-year period around 1250 CE, when observed accumulation rates were the highest in the
35 record.

36 Positive RICE accumulation anomalies have been linked to increased occurrence of eastern
37 Ross Sea/Amundsen Sea blocking events. These blocking events impede the prevailing
38 westerly winds, and direct on-shore winds towards the eastern Ross Sea, which in turn affects
39 the frequency of marine air intrusion, as well as sea-ice distribution and precipitation at RICE
40 and the western Marie Byrd Land regions (Emanuelsson et al., 2017a; Küttel et al., 2012). As
41 eastern Ross Sea/Amundsen blocking is so closely linked to positive RICE accumulation
42 anomalies, a decline in Ross Sea/Amundsen Sea blocking is a likely cause for the recent
43 decline in RICE accumulation. Indeed, there has been several reports of recent strengthening
44 of SAM [e.g., Schneider et al. (2015)] and deepening of the ASL [negative geopotential
45 height trend; e.g. Raphael et al. (2015)], accompanied by reduction of Pacific sector southern
46 hemisphere high-latitude blocking (Oliveira and Ambrizzi, 2017).



1 Linear regression on the derived annual accumulation history shows that accumulation rates at
2 Roosevelt Island since 1950 CE have decreased by an average of 6.6 cm yr^{-1} per century,
3 which is almost 7 times faster than the long-term decreasing trend taking place during the
4 period from 1700 CE to current day (Table 3).

5 **5. Discussion**

6 **5.1. Volcanic detection in low-elevation coastal ice cores**

7 The identification of large tropical volcanic events in the RICE ice core is complicated by the
8 seasonal signal of marine biogenic sulfate, thereby requiring non-traditional methods for the
9 identification and assignment of these events. Whereas most high-elevation (i.e. $>2000 \text{ m}$
10 altitude) ice cores have a sulfate background on the order of 50 ng g^{-1} or less, the equivalent
11 baseline at RICE is closer to 200 ng g^{-1} . Identification of volcanoes therefore relied on non-
12 traditional techniques such as CFA-acidity measurements, along with ECM and calcium-
13 conductivity residuals. Each of these detection methods is effective because they focus on
14 total acidity (H^+ ion concentration) rather than sulfate ion concentration. Emissions from local
15 volcanoes includes relatively short-lived halides such as bromine, chlorine and fluoride,
16 which add to the acidity signal, whereas only sulfate is deposited from distant volcanic
17 eruptions. As a result of focusing on the total acidity, the RICE volcanic record is biased
18 toward local volcanism.

19 An implication of the geographical bias in the RICE volcanic record, combined with the high
20 sulfate background level, is that “typical” large distant volcanic eruptions such as Tambora
21 (1815 CE), Unknown (1809 CE) and Huaynaputina (1600 CE), are all difficult or impossible
22 to identify in the RICE records. The absence of these marker horizons contribute to
23 uncertainty between chronological markers, and it complicates the synchronization of RICE
24 to the many Antarctic ice cores, that have been dated using these eruptions.

25 Volcanic acid deposition markers in the RICE core include Kuwae (131.2 m, 1453 CE) and
26 Samalas (164.06 m, 1257 CE), among others (Table 2). In addition to the volcanic horizons
27 present in other Antarctic cores, we noted several strong volcanic imprints that seemingly
28 have no counterpart in the WAIS Divide ice core data, and thus most likely originate from
29 local West Antarctic volcanoes. An extended list of volcanic eruptions in the RICE core is
30 provided in Table 2.

31 The dipole effect of the Amundsen Sea Low (ASL) may additionally influence the
32 effectiveness by which individual volcanic events are recorded in RICE ice core (Yuan and
33 Martinson, 2000). The ASL dipole acts to direct storm systems either toward the Antarctic
34 Peninsula/Ellsworth Land region, or toward the western Marie Byrd Land/Ross Ice Shelf
35 region (Genthon et al., 2005). Consequently, storm tracks and associated accumulation and
36 wet deposition of ions is strongly controlled by the location of the ASL. This is likely to favor
37 deposition and preservation of volcanic signals in one location (e.g. Antarctic Peninsula) at
38 the expense of the other (RICE, Siple Dome). Absence of sulfate in the RICE core from some
39 of the larger distant volcanic eruptions may be due to a particularly strong ASL state at the
40 time, directing sulfate ions preferentially toward Ellsworth Land and away from Roosevelt
41 Island. This effect is also suggested by synchronization of volcanic peaks between WAIS
42 Divide and RICE ice cores, with regular periods in which synchronization of volcanic
43 indicators is relatively straightforward, and other periods in which synchronization between
44 ice cores is difficult or impossible.



1 Another unusual feature of the RICE volcanic record is that the core contains relatively few
2 visible tephra layers; Only 7 tephra horizons have been identified, of which 6 are within the
3 Holocene section of the core, and only one exists within the last 2700 years (Table 2). This
4 tephra layer (165.02 m depth) corresponds to the 1252 AD eruption of Pleiades in Northern
5 Victoria Land, and was also found in Siple Dome and Taylor Dome ice cores (Dunbar et al.,
6 2003). For comparison, Narcisi et al. (2010) found an average frequency of 1 visible tephra
7 layer per 1000 years in the TALDICE ice core.

8 These challenges of identification and age assignment of volcanoes in the RICE ice core are
9 analogous to the situation at other coastal locations in Antarctica with high background levels
10 of marine sulfate, which can effectively mask the presence of sulfate from distant volcanic
11 eruptions (Philippe et al., 2016; Steig et al., 2005). The RICE volcanic record demonstrates
12 the importance of building an Antarctic-wide network of volcanic reference horizons and the
13 development of non-traditional volcanic detection methods based on acidity. Particular
14 emphasis should be placed on the production of annually-counted timescales, especially as
15 CFA systems become widespread among glaciology laboratories and methods of sufficient
16 resolution are becoming available for relatively high-accumulation Antarctic sites, such as
17 RICE. The importance of a publicly available framework of ice core tephro-stratigraphy and
18 reference datasets for volcanic source provinces is also reaffirmed in this work.

19 **5.2. Diverging regional accumulation trends within West Antarctica**

20 Large regional differences in accumulation trends exist within West Antarctica. In
21 comparison to WAIS Divide (Fig. 9), the RICE accumulation history is much more variable
22 on the centennial scale. Further, the longer-term trends are significantly different between the
23 two locations. At WAIS Divide, accumulation rates were approximately 25% higher 2500
24 years ago and have been declining since, with an acceleration in the rate of decline in the past
25 1000 years. The start of this decline takes place within roughly the same period that also
26 RICE accumulation rates start to decrease. Over the most recent decade (2000-2010),
27 however, WAIS Divide accumulation displays a marked increase in accumulation rates
28 (Thomas et al., 2017), whereas the accumulation at RICE has decreased.

29 The different trends in accumulation rates across West Antarctica may be explained by
30 changes in the strength of the Amundsen Sea Low. The ASL influences accumulation rates in
31 a dipole pattern: negative geopotential height anomalies in the ASL region reduces Amundsen
32 sea blocking, leading to less accumulation over the Ross Ice Shelf area and conversely,
33 greater accumulation over Ellsworth Land (Raphael et al., 2015). The fulcrum of this bipole is
34 located in the vicinity of the West Antarctic ice divide, hence the WAIS Divide ice core
35 should be minimally influenced by the strength of the ASL.

36 Most other coastal Antarctic sites have experienced a significant increase in accumulation
37 rates (10%) since the 1960s, due to a higher frequency in blocking systems that have
38 increased the precipitation in these areas (Frezzotti et al., 2013). The broad similarities and
39 differences noted here raise the question of whether West Antarctic accumulation, as a whole,
40 has been decreasing, or whether the trends represent a redistribution of precipitation. It
41 highlights the problem that only with large spatial coverage, will the current trend in total
42 Antarctic mass balance be elucidated.



1 **5.3. Current mass balance of Roosevelt Island and implications for** 2 **Ross Embayment mass balance**

3 Clausen et al. (1979) estimated the current (1954-1975) accumulation rate at the summit of
4 Roosevelt Island to be $0.20 \text{ m w.e yr}^{-1}$, whereas we here find the current accumulation rate
5 (average of the last 50 years) to be $0.22 \pm 0.06 \text{ m w.e yr}^{-1}$. While these estimates are
6 consistent, we note that the discrepancy between values may be due to the observed high
7 inter-annual variability in accumulation rates. That is, the averaging period of accumulation
8 rates may influence the result. Adding to the challenge is the large spatial gradient in
9 accumulation rates across Roosevelt Island, which means that the location of the
10 measurements is important for estimating the accumulation rate. However, the correlation
11 between annual accumulation rates obtained from the three Roosevelt Island ice cores (RID-
12 75, RICE-12/13-B, RICE main) is high, consistent with the less than 1 km difference between
13 their reported sampling locations.

14 An early mass balance study of the Ross Ice Shelf (Shabtaie and Bentley, 1987) concluded
15 that the ice shelf is in a positive state of mass balance, gaining $38 \pm 12 \text{ km}^3 \text{ yr}^{-1}$, while the
16 upstream inland ice is in a state of negative mass balance: $-23 \pm 15 \text{ km}^3 \text{ yr}^{-1}$. The Ross Ice
17 Shelf primarily gains mass from the inland ice ($111 \pm 4 \text{ km}^3 \text{ yr}^{-1}$) and snow accumulation
18 ($42 \pm 3 \text{ km}^3 \text{ yr}^{-1}$), with snow accumulation therefore accounting for 29% of the total mass gain.
19 With respect to our finding of a 30% decrease in accumulation rates since 1700 CE, we note
20 that sub-shelf processes will be more significant to the overall mass balance of the Ross Ice
21 Shelf in future. The stability of the Ross Ice Shelf may be further threatened by anticipated
22 ocean warming and sea level rise, respectively enhancing subsurface melting and buoyant
23 force on the ice shelf (Joughin and Alley, 2011).

24 **Conclusions**

25 The RICE ice core from Roosevelt Island, Ross Ice Shelf, West Antarctica, was successfully
26 dated back to 700 BCE by annual layer counting based on multiple high-resolution impurity
27 records. The timescale therefore begins after the establishment of an ice divide at Roosevelt
28 Island, and covers most of the time that stable ice divide flow has taken place here. The
29 resulting timescale was validated by volcanic and methane synchronization to WAIS Divide
30 ice core WD2014 chronology, and the two timescales are in excellent agreement. Reliable
31 volcanic match points were difficult to establish, and required the use of new techniques and
32 data sets. This indicates a general challenge for low-altitude ice core sites located close to the
33 open ocean.

34 Correcting for ice flow thinning of annual layers with depth produced an annual accumulation
35 record for Roosevelt Island for the past 2700 years. Accumulation rates were reasonably
36 constant until 1260 CE, after which accumulation rates have consistently decreased. Current
37 accumulation trends at Roosevelt Island indicate a rapid decline of $6.6 \text{ cm w.e per century}$,
38 with a modern accumulation rate of $0.22 \text{ m w.e yr}^{-1}$ (50 year average). This recent trend is
39 similar to that observed at WAIS Divide, although the time of change is earlier at RICE than
40 at WAIS Divide.

41 Layer thickness profiles in the three Roosevelt Island ice cores analyzed here show a high
42 degree of correlation between cores, giving confidence that the RICE core is a reliable climate
43 archive suitable for further understanding of climate and geophysical variability across West
44 Antarctica.



1 **Data availability:**

2 The following data will be made available on the Centre for Ice and Climate website
3 (<http://www.iceandclimate.nbi.ku.dk/data/>) as well as public archives PANGAEA and NOAA
4 paleodatabase: RID-75 isotope and beta-activity records; RICE17 timescale; and RICE
5 accumulation rates.

6

7 **Acknowledgments**

8 This work is a contribution to the Roosevelt Island Climate Evolution (RICE) Program,
9 funded by national contributions from New Zealand, Australia, Denmark, Germany, Italy,
10 China, Sweden, UK and USA. The main logistic support was provided by Antarctica New
11 Zealand (K049) and the US Antarctic Program. We thank all the people involved in the RICE
12 logistics, fieldwork, sampling and analytical programs. The Danish contribution to RICE was
13 funded by the Carlsberg Foundation's North-South Climate Connections project grant. The
14 research also received funding from the European Research Council under the European
15 Community's Seventh Framework Programme (FP7/2007-2013) ERC grant agreement
16 610055 as part of the Ice2Ice project. The RICE Program was supported by funding from
17 NSF grants (PLR-1042883, ANT-0837883, ANT-0944021, ANT-0944307 and ANT-
18 1643394) and New Zealand Ministry of Business, Innovation, and Employment grants issued
19 through Victoria University of Wellington (RDF-VUW-1103, 15-VUW-131), GNS Science
20 (540GCT32, 540GCT12) and Antarctica New Zealand (K049). Figure 1 was made using
21 Quantarctica2 (Norwegian Polar Insitute) basemaps and QGIS software.

22 We present here ice core data collected and analyzed by Henrik Clausen, Willi Dansgaard,
23 Steffen Bo Hansen and Jan Nielsen under the Ross Ice Shelf Project (RISP) carried out
24 between 1973 and 1978. We acknowledge the pioneering work conducted by these
25 researchers and the ongoing international collaborations they established.

26

27 **References**

28 Abbott, P. M., Davies, S. M., Steffensen, J. P., Pearce, N. J. G., Bigler, M., Johnsen, S. J.,
29 Seierstad, I. K., Svensson, A., and Wastegård, S.: A detailed framework of Marine Isotope
30 Stages 4 and 5 volcanic events recorded in two Greenland ice-cores, *Quaternary Sci. Rev.*, 36,
31 59-77, 10.1016/j.quascirev.2011.05.001, 2012.

32 Alley, R. B., Meese, D. A., Shuman, C. A., Gow, A. J., Taylor, K. C., Grootes, P. M., White,
33 J. W. C., Ram, M., Waddington, E. D., Mayewski, P. A., and Zielinski, G. A.: Abrupt
34 increase in Greenland snow accumulation at the end of the Younger Dryas event, *Nature*, 362,
35 527-529, 10.1038/362527a0, 1993.

36 Andersen, K. K., Svensson, A., Rasmussen, S. O., Steffensen, J. P., Johnsen, S. J., Bigler, M.,
37 Röthlisberger, R., Ruth, U., Siggaard-Andersen, M.-L., Dahl-Jensen, D., Vinther, B. M., and
38 Clausen, H. B.: The Greenland Ice Core Chronology 2005, 15-42 ka. Part 1: constructing the
39 time scale, *Quaternary Sci. Rev.*, 25, 3246-3257, 10.1016/j.quascirev.2006.08.002, 2006.

40 Arienzo, M. M., McConnell, J. R., Chellman, N., Criscitiello, A. S., Curran, M., Fritzsche, D.,
41 Kipfstuhl, S., Mulvaney, R., Nolan, M., Opel, T., Sigl, M., and Steffensen, J. P.: A Method



- 1 for Continuous ^{239}Pu Determinations in Arctic and Antarctic Ice Cores, *Environ. Sci.*
2 *Technol.*, 50, 7066-7073, 10.1021/acs.est.6b01108, 2016.
- 3 Bender, M., Sowers, T., Dickson, M.-L., Orchardo, J., Grootes, P., Mayewski, P. A., and
4 Meese, D. A.: Climate correlations between Greenland and Antarctica during the last 100,000
5 years, *Nature*, 372, 663-666, 10.1038/372663a0, 1994.
- 6 Bertler, N. A. N., Conway, H., Dahl-Jensen, D., Emanuelsson, D. B., Winstrup, M.,
7 Vallelonga, P. T., Lee, J. E., Brook, E. J., Severinghaus, J. P., Fudge, T. J., Keller, E. D.,
8 Baisden, W. T., Hindmarsh, R. C. A., Neff, P. D., Blunier, T., Edwards, R., Mayewski, P. A.,
9 Kipfstuhl, S., Buizert, C., Canessa, S., Dacic, R., Kjær, H. A., Kurbatov, A., Zhang, D.,
10 Waddington, E. D., Baccolo, G., Beers, T., Brightley, H. J., Carter, L., Clemens-Sewall, D.,
11 Ciobanu, V. G., Delmonte, B., Eling, L., Ellis, A. A., Ganesh, S., Golledge, N. R., Haines, S.
12 A., Handley, M., Hawley, R. L., Hogan, C. M., Johnson, K. M., Korotkikh, E., Lowry, D. P.,
13 Mandeno, D., McKay, R. M., Menking, J. A., Naish, T. R., Noerling, C., Ollive, A., Orsi, A.,
14 Proemse, B. C., Pyne, A. R., Pyne, R. L., Renwick, J., Scherer, R. P., Semper, S., Simonsen,
15 M., Sneed, S. B., Steig, E. J., Tuohy, A., Ulayottil Venugopal, A., Valero-Delgado, F.,
16 Venkatesh, J., Wang, F., Wang, S., Winski, D. A., Winton, V. H. L., Whiteford, A., Xiao, C.,
17 Yang, J., and Zhang, X.: The Ross Sea Dipole - Temperature, Snow Accumulation and Sea
18 Ice Variability in the Ross Sea Region, Antarctica, over the Past 2,700 Years, *Clim. Past*
19 *Discuss.*, 2017, 1-31, 10.5194/cp-2017-95, 2017.
- 20 Bigler, M., Svensson, A., Kettner, E., Vallelonga, P., Nielsen, M., and Steffensen, J. P.:
21 Optimization of High-Resolution Continuous Flow Analysis for Transient Climate Signals in
22 Ice Cores, *Environ. Sci. Technol.*, 45, 4483-4489, 10.1021/es200118j, 2011.
- 23 Blunier, T., Chappellaz, J., Schwander, J., Dällenbach, A., Stauffer, B., Stocker, T. F.,
24 Raynaud, D., Jouzel, J., Clausen, H. B., Hammer, C. U., and Johnsen, S. J.: Asynchrony of
25 Antarctic and Greenland climate change during the last glacial period, *Nature*, 394, 739-743,
26 10.1038/29447, 1998.
- 27 Blunier, T., and Brook, E. J.: Timing of millennial-scale climate change in Antarctica and
28 Greenland during the last glacial period, *Science*, 291, 109-112,
29 10.1126/science.291.5501.109, 2001.
- 30 Buizert, C., Cuffey, K. M., Severinghaus, J. P., Baggenstos, D., Fudge, T. J., Steig, E. J.,
31 Markle, B. R., Winstrup, M., Rhodes, R. H., Brook, E. J., Sowers, T. A., Clow, G. D., Cheng,
32 H., Edwards, R. L., Sigl, M., McConnell, J. R., and Taylor, K. C.: The WAIS Divide deep ice
33 core WD2014 chronology - Part 1: Methane synchronization (68–31 ka BP) and the gas age–
34 ice age difference, *Clim. Past*, 11, 153-173, 10.5194/cp-11-153-2015, 2015.
- 35 Clausen, H. B., Dansgaard, W., Nielsen, J. O., and Clough, J. W.: Surface accumulation on
36 Ross Ice Shelf, *Antarctic Journal of the United States*, 14, 68-71, 1979.
- 37 Conway, H., Hall, B. L., Denton, G. H., Gades, A. M., and Waddington, E. D.: Past and
38 Future Grounding-Line Retreat of the West Antarctic Ice Sheet, *Science*, 286, 280,
39 10.1126/science.286.5438.280, 1999.
- 40 Dahl-Jensen, D., Johnsen, S. J., Hammer, C. U., Clausen, H. B., and Jouzel, J.: Past
41 accumulation rates derived from observed annual layers in the GRIP ice core from Summit,



- 1 Central Greenland, in: *Ice in the Climate System*, edited by: Peltier, R. W., NATO ASI Ser. I,
2 Springer-Verlag, New York, 517-532, 1993.
- 3 Davies, S. M., Wastegård, S., Abbott, P. M., Barbante, C., Bigler, M., Johnsen, S. J.,
4 Rasmussen, T. L., Steffensen, J. P., and Svensson, A.: Tracing volcanic events in the NGRIP
5 ice-core and synchronising North Atlantic marine records during the last glacial period, *Earth
6 Planet. Sci. Lett.*, 294, 69-79, 10.1016/j.epsl.2010.03.004, 2010.
- 7 Dee, D. P., Uppala, S. M., Simmons, A. J., Berrisford, P., Poli, P., Kobayashi, S., Andrae, U.,
8 Balmaseda, M. A., Balsamo, G., Bauer, P., Bechtold, P., Beljaars, A. C. M., van de Berg, L.,
9 Bidlot, J., Bormann, N., Delsol, C., Dragani, R., Fuentes, M., Geer, A. J., Haimberger, L.,
10 Healy, S. B., Hersbach, H., Hólm, E. V., Isaksen, I., Kållberg, P., Köhler, M., Matricardi, M.,
11 McNally, A. P., Monge-Sanz, B. M., Morcrette, J. J., Park, B. K., Peubey, C., de Rosnay, P.,
12 Tavolato, C., Thépaut, J. N., and Vitart, F.: The ERA-Interim reanalysis: configuration and
13 performance of the data assimilation system, *Quarterly Journal of the Royal Meteorological
14 Society*, 137, 553-597, 10.1002/qj.828, 2011.
- 15 Dunbar, N. W., Zielinski, G. A., and Voisins, D. T.: Tephra layers in the Siple Dome and
16 Taylor Dome ice cores, Antarctica: Sources and correlations, *Journal of Geophysical
17 Research: Solid Earth*, 108, 10.1029/2002JB002056, 2003.
- 18 Emanuelsson, B. D., Baisden, W. T., Bertler, N. A. N., Keller, E. D., and Gkinis, V.: High-
19 resolution continuous-flow analysis setup for water isotopic measurement from ice cores
20 using laser spectroscopy, *Atmos. Meas. Tech.*, 8, 2869-2883, 10.5194/amt-8-2869-2015,
21 2015.
- 22 Emanuelsson, B. D., Neff, P. D., Bertler, N. A. N., Markle, B. R., Renwick, J. A., Baisden,
23 W. T., and Keller, E. D.: Southern Hemisphere ENSO-SAM dynamics captured in water
24 isotopes (δD) from the Roosevelt Island Climate Evolution (RICE) ice core, Antarctica, *J.
25 Geophys. Res.-Atmos.*, in preparation, 2017a.
- 26 Emanuelsson, B. D., Bertler, N. A. N., Neff, P. D., Markle, B. R., W.T., B., and E., K.: The
27 role of Amundsen-Bellinghousen Sea anticyclonic circulation in forcing marine air intrusions
28 into West Antarctica, *Clim. Dyn.*, submitted, 2017b.
- 29 EPICA community members: One-to-one coupling of glacial climate variability in Greenland
30 and Antarctica, *Nature*, 444, 195-198, 10.1038/nature05301, 2006.
- 31 Ferretti, D. F., Miller, J. B., White, J. W. C., Etheridge, D. M., Lassey, K. R., Lowe, D. C., C.
32 M. MacFarling Meure, Dreier, M. F., Trudinger, C. M., T. D. van Ommen, and Langenfelds,
33 R. L.: Unexpected changes to the global methane budget over the past 2000 years, *Science*,
34 309, 1714-1717, 10.1126/science.1115193, 2005.
- 35 Frezzotti, M., Urbini, S., Proposito, M., Scarchilli, C., and Gandolfi, S.: Spatial and temporal
36 variability of surface mass balance near Talos Dome, East Antarctica, *Journal of Geophysical
37 Research: Earth Surface*, 112, 10.1029/2006JF000638, 2007.
- 38 Frezzotti, M., Scarchilli, C., Becagli, S., Proposito, M., and Urbini, S.: A synthesis of the
39 Antarctic surface mass balance during the last 800 yr, *The Cryosphere*, 7, 303-319,
40 10.5194/tc-7-303-2013, 2013.



- 1 Frieler, K., Clark, P. U., He, F., Buizert, C., Reese, R., Ligtenberg, S. R. M., van den Broeke,
2 M. R., Winkelmann, R., and Levermann, A.: Consistent evidence of increasing Antarctic
3 accumulation with warming, *Nature Clim. Change*, 5, 348-352, 10.1038/nclimate2574, 2015.
- 4 Frieß, U., Deutschmann, T., Gilfedder, B. S., Weller, R., and Platt, U.: Iodine monoxide in the
5 Antarctic snowpack, *Atmos. Chem. Phys.*, 10, 2439-2456, 10.5194/acp-10-2439-2010, 2010.
- 6 Gabrieli, J., Cozzi, G., Vallelonga, P., Schwikowski, M., Sigl, M., Eickenberg, J., Wacker, L.,
7 Boutron, C., Gaggeler, H., Cescon, P., and Barbante, C.: Contamination of Alpine snow and
8 ice at Colle Gnifetti, Swiss/Italian Alps, from nuclear weapons tests, *Atmos. Environ.*, 45,
9 587-593, 10.1016/j.atmosenv.2010.10.039, 2011.
- 10 Genthon, C., Kaspari, S., and Mayewski, P. A.: Interannual variability of the surface mass
11 balance of West Antarctica from ITASE cores and ERA40 reanalyses, 1958–2000, *Clim.
12 Dyn.*, 24, 759-770, 10.1007/s00382-005-0019-2, 2005.
- 13 Hammer, C. U.: Acidity of polar ice cores in relation to absolute dating, past volcanism, and
14 radio-echoes, *J. Glaciol.*, 25, 359-372, 10.1017/S0022143000015227, 1980.
- 15 Herron, M. M., and Langway, C. C., Jr.: Firn densification: An empirical model, *J. Glaciol.*,
16 25, 373-385, 10.1017/S0022143000015239, 1980.
- 17 Huybers, P.: Depth and orbital tuning : a new chronology of glaciation and nonlinear orbital
18 climate change, MSc, Dept. of Earth, Atmospheric, and Planetary Sciences., Massachusetts
19 Institute of Technology, 121 pp., 2002.
- 20 Joughin, I., and Alley, R. B.: Stability of the West Antarctic ice sheet in a warming world,
21 *Nature Geosci*, 4, 506-513, 10.1038/ngeo1194, 2011.
- 22 Kingslake, J., Hindmarsh, R. C. A., Aðalgeirsdóttir, G., Conway, H., Corr, H. F. J., Gillet-
23 Chautet, F., Martín, C., King, E. C., Mulvaney, R., and Pritchard, H. D.: Full-depth englacial
24 vertical ice sheet velocities measured using phase-sensitive radar, *Journal of Geophysical
25 Research: Earth Surface*, 119, 2604-2618, 10.1002/2014JF003275, 2014.
- 26 Kjær, H. A., Vallelonga, P., Svensson, A., Elleskov L. Kristensen, M., Tibuleac, C.,
27 Winstrup, M., and Kipfstuhl, S.: An Optical Dye Method for Continuous Determination of
28 Acidity in Ice Cores, *Environ. Sci. Technol.*, 10.1021/acs.est.6b00026, 2016.
- 29 Kurbatov, A. V., Zielinski, G. A., Dunbar, N. W., Mayewski, P. A., Meyerson, E. A., Sneed,
30 S. B., and Taylor, K. C.: A 12,000 year record of explosive volcanism in the Siple Dome Ice
31 Core, West Antarctica, *Journal of Geophysical Research: Atmospheres*, 111,
32 10.1029/2005JD006072, 2006.
- 33 Küttel, M., Steig, E. J., Ding, Q., Monaghan, A. J., and Battisti, D. S.: Seasonal climate
34 information preserved in West Antarctic ice core water isotopes: relationships to temperature,
35 large-scale circulation, and sea ice, *Clim. Dyn.*, 39, 1841-1857, 10.1007/s00382-012-1460-7,
36 2012.
- 37 Lee, J. E., Brook, E. J., Severinghaus, J. P., Blunier, T., Buizert, C., Fudge, T. J., Conway, H.,
38 Waddington, E. D., Parrenin, F., Dahl-Jensen, D., Winstrup, M., Vallelonga, P., Ciobanu, G.,
39 and Bertler, N.: An 83,000 year old ice core from Roosevelt Island, Ross Sea, Antarctica,
40 *Clim. Past Discuss.*, in preparation, 2017.



- 1 Legrand, M., Feniet-Saigne, C., Saltzman, E. S., Germain, C., Barkov, N. I., and Petrov, V.
2 N.: Ice-core record of oceanic emissions of dimethylsulphide during the last climatic cycle,
3 *Nature*, 350, 144-146, 10.1038/350144a0, 1991.
- 4 Lliboutry, L.: A critical review of analytical approximate solutions for steady state velocities
5 and temperatures in cold ice-sheets, *Zeitschrift für Gletscherkunde und Glazialgeologie*, 15,
6 135-148, 1979.
- 7 Martín, C., Hindmarsh, R. C. A., and Navarro, F. J.: Dating ice flow change near the flow
8 divide at Roosevelt Island, Antarctica, by using a thermomechanical model to predict radar
9 stratigraphy, *Journal of Geophysical Research: Earth Surface*, 111, 10.1029/2005JF000326,
10 2006.
- 11 Medley, B., Joughin, I., Das, S. B., Steig, E. J., Conway, H., Gogineni, S., Criscitiello, A. S.,
12 McConnell, J. R., Smith, B. E., van den Broeke, M. R., Lenaerts, J. T. M., Bromwich, D. H.,
13 and Nicolas, J. P.: Airborne-radar and ice-core observations of annual snow accumulation
14 over Thwaites Glacier, West Antarctica confirm the spatiotemporal variability of global and
15 regional atmospheric models, *Geophys. Res. Lett.*, 40, 3649-3654, 10.1002/grl.50706, 2013.
- 16 Mitchell, L., Brook, E., Lee, J. E., Buizert, C., and Sowers, T.: Constraints on the Late
17 Holocene Anthropogenic Contribution to the Atmospheric Methane Budget, *Science*, 342,
18 964, 10.1126/science.1238920, 2013.
- 19 Mitchell, L. E., Brook, E. J., Sowers, T., McConnell, J. R., and Taylor, K.: Multidecadal
20 variability of atmospheric methane, 1000–1800 C.E, *Journal of Geophysical Research:*
21 *Biogeosciences*, 116, n/a-n/a, 10.1029/2010JG001441, 2011.
- 22 Narcisi, B., Proposito, M., and Frezzotti, M.: Ice record of a 13th century explosive volcanic
23 eruption in northern Victoria Land, East Antarctica, *Antarctic Science*, 13, 174-181,
24 10.1017/S0954102001000268, 2001.
- 25 Narcisi, B., Petit, J. R., and Chappellaz, J.: A 70 ka record of explosive eruptions from the
26 TALDICE ice core (Talos Dome, East Antarctic plateau), *Journal of Quaternary Science*, 25,
27 844-849, 10.1002/jqs.1427, 2010.
- 28 Nye, J. F.: Correction factor for accumulation measured by the thickness of the annual layers
29 in an ice sheet, *J. Glaciol.*, 4, 785-788, 10.1017/S0022143000028367, 1963.
- 30 Oliveira, F. N. M., and Ambrizzi, T.: The effects of ENSO-types and SAM on the large-scale
31 southern blockings, *International Journal of Climatology*, 37, 3067–3081, 10.1002/joc.4899,
32 2017.
- 33 Philippe, M., Tison, J. L., Fjøsne, K., Hubbard, B., Kjær, H. A., Lenaerts, J. T. M., Drews, R.,
34 Sheldon, S. G., De Bondt, K., Claeys, P., and Pattyn, F.: Ice core evidence for a 20th century
35 increase in surface mass balance in coastal Dronning Maud Land, East Antarctica, *The*
36 *Cryosphere*, 10, 2501-2516, 10.5194/tc-10-2501-2016, 2016.
- 37 Rabiner, L. R.: A tutorial on hidden Markov models and selected applications in speech
38 recognition, *Proceedings of the IEEE*, 77, 257-286, 10.1109/5.18626, 1989.
- 39 Raphael, M. N., Marshall, G. J., Turner, J., Fogt, R., Schneider, D., Dixon, D. A., Hosking, J.
40 S., Jones, J. M., and Hobbs, W. R.: The Amundsen Sea Low: Variability, Change and Impact



- 1 on Antarctic Climate, *Bull. Am. Meteorol. Soc.*, 150331122920005, 10.1175/BAMS-D-14-
2 00018.1, 2015.
- 3 Rasmussen, S. O., Vinther, B. M., Clausen, H. B., and Andersen, K. K.: Early Holocene
4 climate oscillations recorded in three Greenland ice cores, *Quaternary Sci. Rev.*, 26, 1907-
5 1914, 10.1016/j.quascirev.2007.06.015, 2007.
- 6 Rasmussen, S. O., Bigler, M., Blockley, S. P., Blunier, T., Buchardt, S. L., Clausen, H. B.,
7 Cvijanovic, I., Dahl-Jensen, D., Johnsen, S. J., Fischer, H., Gkinis, V., Guillevic, M., Hoek,
8 W. Z., Lowe, J. J., Pedro, J. B., Popp, T., Seierstad, I. K., Steffensen, J. P., Svensson, A. M.,
9 Vallelonga, P., Vinther, B. M., Walker, M. J. C., Wheatley, J. J., and Winstrup, M.: A
10 stratigraphic framework for abrupt climatic changes during the Last Glacial period based on
11 three synchronized Greenland ice-core records: refining and extending the INTIMATE event
12 stratigraphy, *Quaternary Sci. Rev.*, 106, 14-28, 10.1016/j.quascirev.2014.09.007, 2014.
- 13 Raymond, C. F.: Deformation in the vicinity of ice divides, *J. Glaciol.*, 29, 357-373,
14 10.1017/S0022143000030288, 1983.
- 15 Schlosser, E., Stenni, B., Valt, M., Cagnati, A., Powers, J. G., Manning, K. W., Raphael, M.,
16 and Duda, M. G.: Precipitation and synoptic regime in two extreme years 2009 and 2010 at
17 Dome C, Antarctica – implications for ice core interpretation, *Atmos. Chem. Phys.*, 16, 4757-
18 4770, 10.5194/acp-16-4757-2016, 2016.
- 19 Schneider, D. P., Deser, C., and Fan, T.: Comparing the Impacts of Tropical SST Variability
20 and Polar Stratospheric Ozone Loss on the Southern Ocean Westerly Winds, *Journal of*
21 *Climate*, 28, 9350–9372, 10.1175/JCLI-D-15-0090.1, 2015.
- 22 Schwander, J., and Stauffer, B.: Age difference between polar ice and the air trapped in its
23 bubbles, *Nature*, 311, 45-47, 10.1038/311045a0, 1984.
- 24 Severinghaus, J. P., Beaudette, R., Headly, M. A., Taylor, K., and Brook, E. J.: Oxygen-18 of
25 O₂ Records the Impact of Abrupt Climate Change on the Terrestrial Biosphere, *Science*, 324,
26 1431, 10.1126/science.1169473, 2009.
- 27 Shabtaie, S., and Bentley, C. R.: West Antarctic ice streams draining into the Ross Ice Shelf:
28 Configuration and mass balance, *Journal of Geophysical Research: Solid Earth*, 92, 1311-
29 1336, 10.1029/JB092iB02p01311, 1987.
- 30 Shepherd, A., Ivins, E. R., A, G., Barletta, V. R., Bentley, M. J., Bettadpur, S., Briggs, K. H.,
31 Bromwich, D. H., Forsberg, R., Galin, N., Horwath, M., Jacobs, S., Joughin, I., King, M. A.,
32 Lenaerts, J. T. M., Li, J., Ligtenberg, S. R. M., Luckman, A., Luthcke, S. B., McMillan, M.,
33 Meister, R., Milne, G., Mouginito, J., Muir, A., Nicolas, J. P., Paden, J., Payne, A. J.,
34 Pritchard, H., Rignot, E., Rott, H., Sørensen, L. S., Scambos, T. A., Scheuchl, B., Schrama, E.
35 J. O., Smith, B., Sundal, A. V., van Angelen, J. H., van de Berg, W. J., van den Broeke, M.
36 R., Vaughan, D. G., Velicogna, I., Wahr, J., Whitehouse, P. L., Wingham, D. J., Yi, D.,
37 Young, D., and Zwally, H. J.: A Reconciled Estimate of Ice-Sheet Mass Balance, *Science*,
38 338, 1183, 10.1126/science.1228102, 2012.
- 39 Sigl, M., Winstrup, M., McConnell, J. R., Welten, K. C., Plunkett, G., Ludlow, F., Buntgen,
40 U., Caffee, M., Chellman, N., Dahl-Jensen, D., Fischer, H., Kipfstuhl, S., Kostick, C.,
41 Maselli, O. J., Mekhaldi, F., Mulvaney, R., Muscheler, R., Pasteris, D. R., Pilcher, J. R.,
42 Salzer, M., Schupbach, S., Steffensen, J. P., Vinther, B. M., and Woodruff, T. E.: Timing and



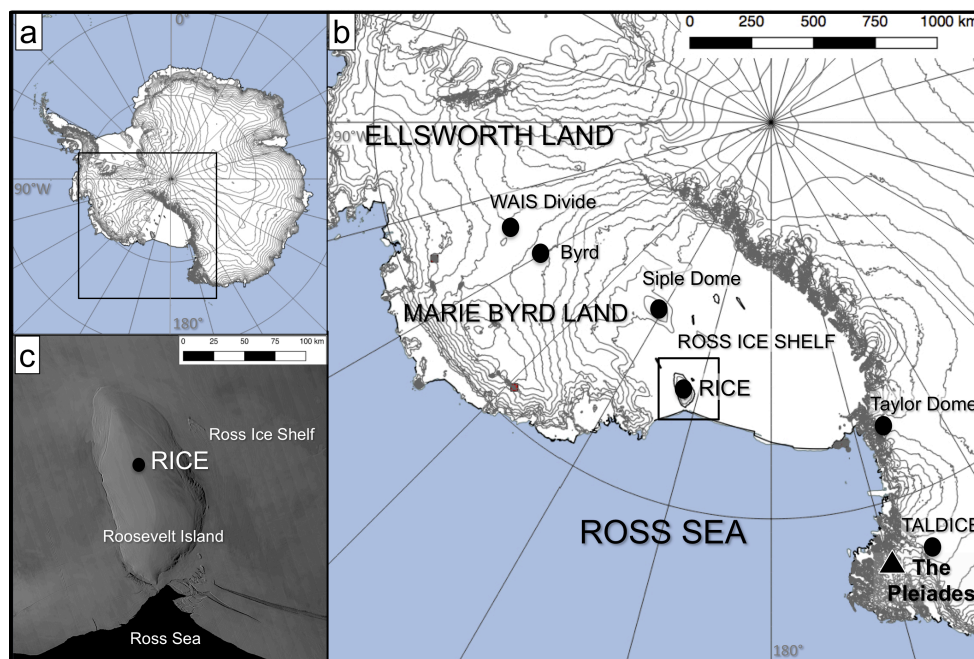
- 1 climate forcing of volcanic eruptions for the past 2,500 years, *Nature*, 523, 543-549,
2 10.1038/nature14565, 2015.
- 3 Sigl, M., Fudge, T. J., Winstrup, M., Cole-Dai, J., Ferris, D., McConnell, J. R., Taylor, K. C.,
4 Welten, K. C., Woodruff, T. E., Adolphi, F., Bisiaux, M., Brook, E. J., Buizert, C., Caffee, M.
5 W., Dunbar, N. W., Edwards, R., Geng, L., Iverson, N., Koffman, B., Layman, L., Maselli, O.
6 J., McGwire, K., Muscheler, R., Nishiizumi, K., Pasteris, D. R., Rhodes, R. H., and Sowers,
7 T. A.: The WAIS Divide deep ice core WD2014 chronology - Part 2: Annual-layer counting
8 (0-31 ka BP), *Clim. Past*, 12, 769-786, 10.5194/cp-12-769-2016, 2016.
- 9 Steig, E. J., Mayewski, P. A., Dixon, D. A., Kaspari, S. D., Frey, M. M., Schneider, D. P.,
10 Arcone, S. A., Hamilton, G. S., Spikes, V. B., Albert, M., Meese, D., Gow, A. J., Shuman, C.
11 A., White, J. W. C., Sneed, S. B., Flaherty, J., and Wumkes, M.: High-resolution ice cores
12 from US ITASE (West Antarctica): development and validation of chronologies and
13 determination of precision and accuracy, *Ann. Glaciol.*, 41, 77-84,
14 10.3189/172756405781813311, 2005.
- 15 Stenni, B., Curran, M. A. J., Abram, N. J., Orsi, A., Goursaud, S., Masson-Delmotte, V.,
16 Neukom, R., Goosse, H., Divine, D., van Ommen, T., Steig, E. J., Dixon, D. A., Thomas, E.
17 R., Bertler, N. A. N., Isaksson, E., Ekaykin, A., Frezzotti, M., and Werner, M.: Antarctic
18 climate variability at regional and continental scales over the last 2,000 years, *Clim. Past*
19 *Discuss.*, 2017, 1-35, 10.5194/cp-2017-40, 2017.
- 20 Stowasser, C., Buizert, C., Gkinis, V., Chappelaz, J., Schüpbach, S., Bigler, M., Faïn, X.,
21 Sperlich, P., Baumgartner, M., Schilt, A., and Blunier, T.: Continuous measurements of
22 methane mixing ratios from ice cores, *Atmos. Meas. Tech.*, 5, 999-1013, 10.5194/amt-5-999-
23 2012, 2012.
- 24 Svensson, A., Andersen, K. K., Bigler, M., Clausen, H. B., Dahl-Jensen, D., Davies, S. M.,
25 Johnsen, S. J., Muscheler, R., Parrenin, F., Rasmussen, S. O., Röthlisberger, R., Seierstad, I.,
26 Steffensen, J. P., and Vinther, B. M.: A 60 000 year Greenland stratigraphic ice core
27 chronology, *Clim. Past*, 4, 47-57, 10.5194/cp-4-47-2008, 2008.
- 28 Svensson, A., Fujita, S., Bigler, M., Braun, M., Dallmayr, R., Gkinis, V., Goto-Azuma, K.,
29 Hirabayashi, M., Kawamura, K., Kipfstuhl, S., Kjörboe, H. A., Popp, T., Simonsen, M.,
30 Steffensen, J. P., Vallenga, P., and Vinther, B. M.: On the occurrence of annual layers in
31 Dome Fuji ice core early Holocene ice, *Clim. Past Discuss.*, 11, 805-830, 10.5194/cpd-11-
32 805-2015, 2015.
- 33 Taylor, K. C., Alley, R. B., Meese, D. A., Spencer, M. K., Brook, E. J., Dunbar, N. W.,
34 Finkel, R. C., Gow, A. J., Kurbatov, A. V., Lamorey, G. W., Mayewski, P. A., Meyerson, E.
35 A., Nishizumi, K., and Zielinski, G. A.: Dating the Siple Dome (Antarctica) ice core by
36 manual and computer interpretation of annual layering, *J. Glaciol.*, 50, 453-461,
37 10.3189/172756504781829864, 2004.
- 38 Thomas, E. R., van Wessem, J. M., Roberts, J., Isaksson, E., Schlosser, E., Fudge, T.,
39 Vallenga, P., Medley, B., Lenaerts, J., Bertler, N., van den Broeke, M. R., Dixon, D. A.,
40 Frezzotti, M., Stenni, B., Curran, M., and Ekaykin, A. A.: Review of regional Antarctic snow
41 accumulation over the past 1000 years, *Clim. Past Discuss.*, 2017, 1-42, 10.5194/cp-2017-18,
42 2017.



- 1 Traversi, R., Becagli, S., Castellano, E., Maggi, V., Morganti, A., Severi, M., and Udisti, R.:
2 Ultra-sensitive Flow Injection Analysis (FIA) determination of calcium in ice cores at ppt
3 level, *Analytica Chimica Acta*, 594, 219-225, 10.1016/j.aca.2007.05.022, 2007.
- 4 Udisti, R., Traversi, R., Becagli, S., and Piccardi, G.: Spatial distribution and seasonal pattern
5 of biogenic sulphur compounds in snow from northern Victoria Land, Antarctica, *Ann.*
6 *Glaciol.*, 27, 535-542, 10.1017/S0260305500018024, 1998.
- 7 Wais Divide Project Members: Onset of deglacial warming in West Antarctica driven by local
8 orbital forcing, *Nature*, 500, 440-444, 10.1038/nature12376, 2013.
- 9 Wais Divide Project Members: Precise inter-polar phasing of abrupt climate change during the
10 last ice age, *Nature*, 520, 661-665, 10.1038/nature14401, 2015.
- 11 Winstrup, M., Svensson, A. M., Rasmussen, S. O., Winther, O., Steig, E. J., and Axelrod, A.
12 E.: An automated approach for annual layer counting in ice cores, *Clim. Past*, 8, 1881-1895,
13 10.5194/cp-8-1881-2012, 2012.
- 14 Winstrup, M.: A Hidden Markov Model Approach to Infer Timescales for High-Resolution
15 Climate Archives, Proceedings of the 30th AAAI Conference on Artificial Intelligence and
16 the 28th Innovative Applications of Artificial Intelligence Conference. February 12 – 17,
17 2016, Phoenix, Arizona USA, AAAI Press, Palo Alto, California, 4053 pp., 2016.
- 18 Yuan, X., and Martinson, D. G.: Antarctic Sea Ice Extent Variability and Its Global
19 Connectivity, *Journal of Climate*, 13, 1697-1717, 10.1175/1520-
20 0442(2000)013<1697:ASIEVA>2.0.CO;2, 2000.
- 21 Zreda-Gostynka, G., Kyle, P. R., Finnegan, D., and Prestbo, K. M.: Volcanic gas emissions
22 from Mount Erebus and their impact on the Antarctic environment, *J. Geophys. Res.*, 102,
23 15039-15055, 10.1029/97JB00155, 1997.
- 24

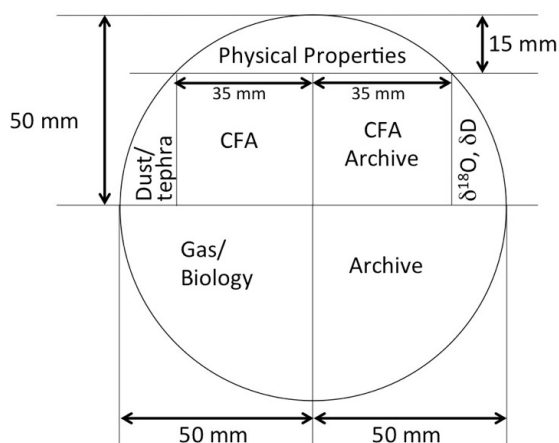


1 **Figures**



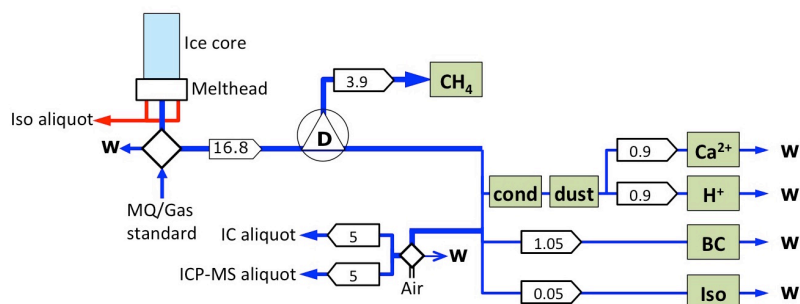
2
3
4

5 **Figure 1:** a, b): Roosevelt Island is located in the eastern margin of the Ross Ice Shelf
 6 embayment. Locations discussed in the text are represented by triangles (volcanoes) or circles
 7 (ice-cores). c) MODIS image of Roosevelt Island (Haran et al. 2013), which protrudes as an
 8 ice dome from the surrounding Ross Ice Shelf. The RICE ice core is drilled on the ice divide
 9 of Roosevelt Island.



10

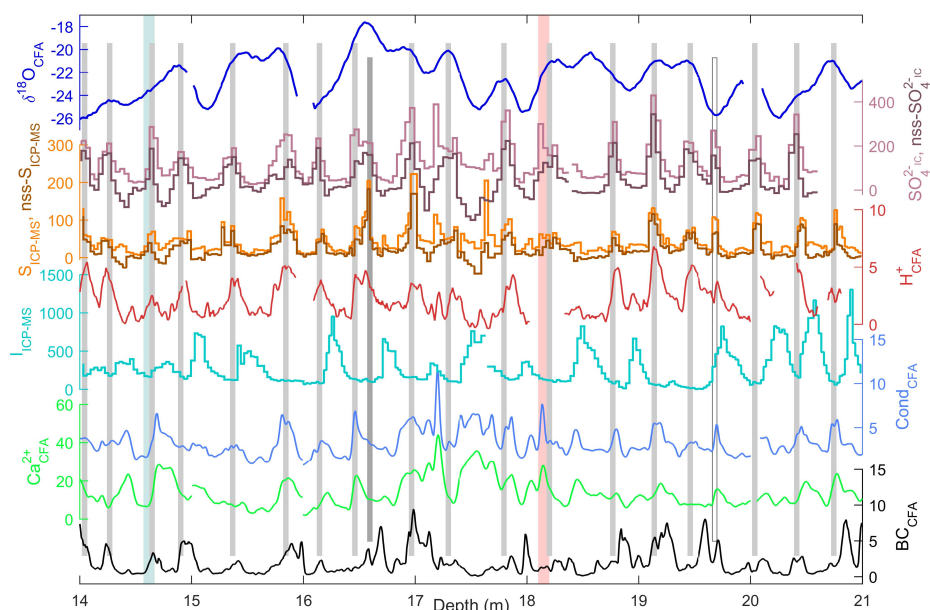
11 **Figure 2:** The RICE main core cutting plan included 2 CFA sticks of size 35x35mm.



1

2 **Figure 3:** CFA set-up for analysis of the RICE core. A 1-m long ice-core rod (light blue) is
 3 placed on a melt head, which separates melt water from the pristine inner part of the core
 4 from that of the more contaminated outer rim. Meltwater from the outer stream (red) is used
 5 for discrete measurements of water isotopes, while the melt water stream from the inner core
 6 section (dark blue) passes through a debubbler (D), which separates air from the melt water.
 7 The air composition is analyzed for methane concentration, while the meltwater stream is
 8 channeled to various analytical instruments for continuous impurity analysis of dust,
 9 conductivity (cond), calcium (Ca²⁺), acidity (H⁺), black carbon (BC), and water isotopes (Iso),
 10 as well as collected in vials for discrete aliquot sampling by IC and ICP-MS. W denotes waste
 11 water. Diamonds represent injection valves used for introduction of air or water standards
 12 when the melter system is not in use. Arrow boxes indicate liquid flow rates in mL min⁻¹.
 13 Green boxes represent analytical instruments.

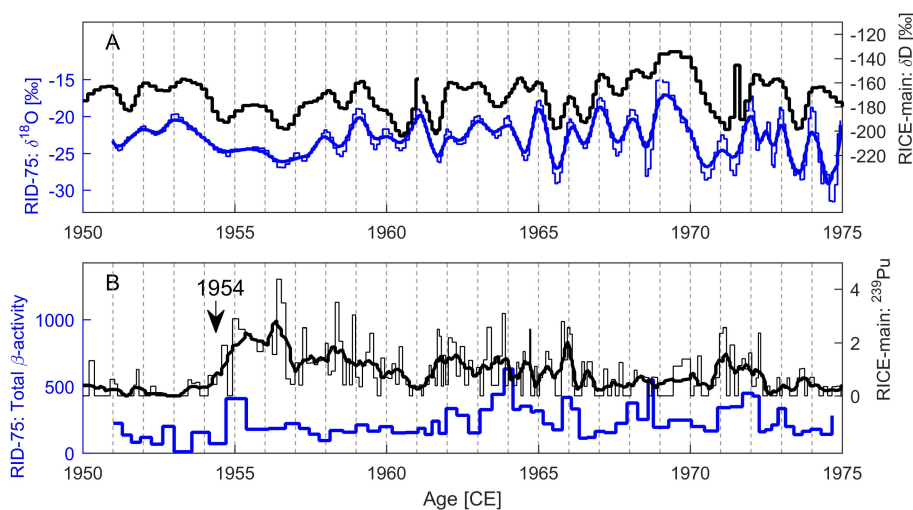
14



1

2 **Figure 4:** Assignment of annual layers in an upper section of the RICE core. All units are in
3 ppb, except for $\delta^{18}\text{O}$ (in ‰), H^+ (in $\mu\text{eq L}^{-1}$), and conductivity (in $\mu\text{S cm}^{-1}$). The CFA
4 chemistry records are smoothed with a 3-cm moving average filter. Two uncertain layers exist
5 within the displayed section: At 16.6 m, an uncertain layer is being counted as part of the
6 timescale, in order to match the tiepoint ages corresponding to the isotope match to RID-75
7 (cyan bar; 14.6 m) and the Raoul tephra horizon (red bar; 18.1 m). A second uncertain layer is
8 located at 19.7 m; the sulfate record suggest that it is an annual layer, but this is not supported
9 by iodine and $\delta^{18}\text{O}$. This layer is not counted in the RICE17 chronology, in order to match the
10 age of the next tie-point located at 22 m.

11



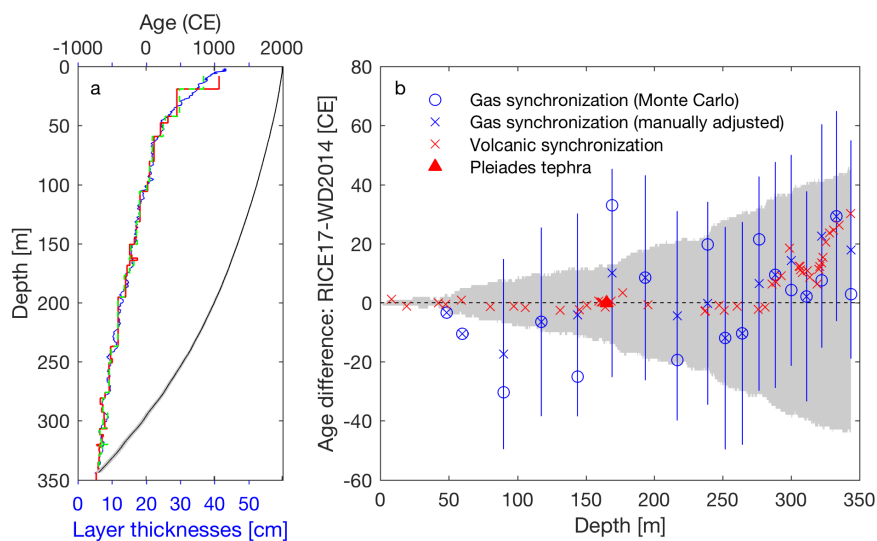
1

2 **Figure 5:** A) RICE water isotope profile (δD) compared to isotope data ($\delta^{18}\text{O}$) from the old
3 RID-75 core for the period 1950-1975. Diffusion causes the isotope record to smooth over
4 time, and a smoothed version of the RID-75 isotope profile (thick blue) highlights its
5 similarities to the RICE isotope record. B) Total specific β -activity (in disintegrations per
6 hour, dph) for the RID-75 core compared to ^{239}Pu measurements (normalized intensities) from
7 the RICE main core. Both cores show a sharp increase in nuclear waste deposition starting in
8 1954CE, and several broader peaks hereafter.

9



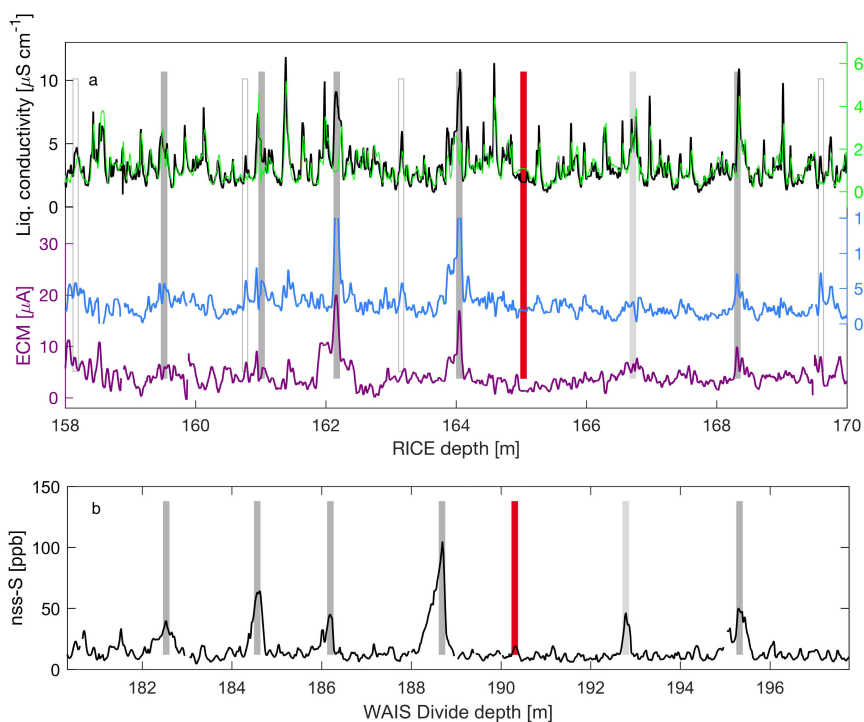
1
2
3



4
5

6 **Figure 6:** a) The RICE17 timescale with depth, including the associated 95% confidence
7 interval (grey area, almost invisible due to scale), and the depth evolution in mean layer
8 thicknesses (50 year running mean; blue). Red stepped line shows the annual layer
9 thicknesses derived from volcanic match points. b) RICE17 and its corresponding 95% age
10 confidence interval (grey area) compared to WD2014 from volcanic (red) and methane (blue)
11 synchronization to the WAIS Divide core. The solid red triangle indicates the Pleiades tephra
12 layer at 165m depth. A positive age difference implies fewer layers in the RICE17 timescale
13 than in WD2014.

14
15



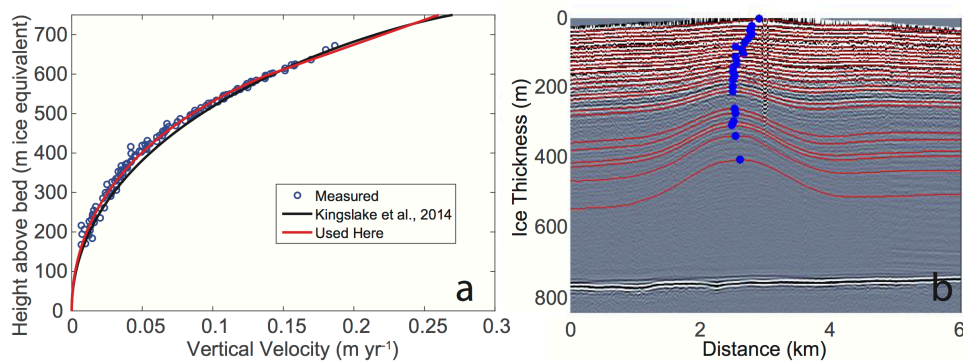
1

2 **Figure 7:** a) The RICE volcanic records: ECM (purple), acidity (blue), and calcium-to-
3 conductivity relation (black and green), and their synchronization to b) the WAIS Divide non-
4 sea-salt sulfur record (Sigl et al., 2015). Solid vertical bars indicate common volcanic match
5 points (Table 2). The red bar signifies the Pleiades tephra horizon (1252 CE), found in both
6 cores. Dark grey bars are volcanic match points that are clearly expressed in both cores. In the
7 RICE core, these can be found as a peak in the acidity record as well as significantly
8 enhanced conductivity levels compared to the sea-salt influx recorded via the calcium record.
9 The light grey bar is a potential volcanic match between the two cores that was not used for
10 validation of the timescale. RICE occasionally shows indications of volcanic activity (white
11 bars), for which no counterpart exist in the WAIS Divide core.

12



1



2

3

4

5

6

7

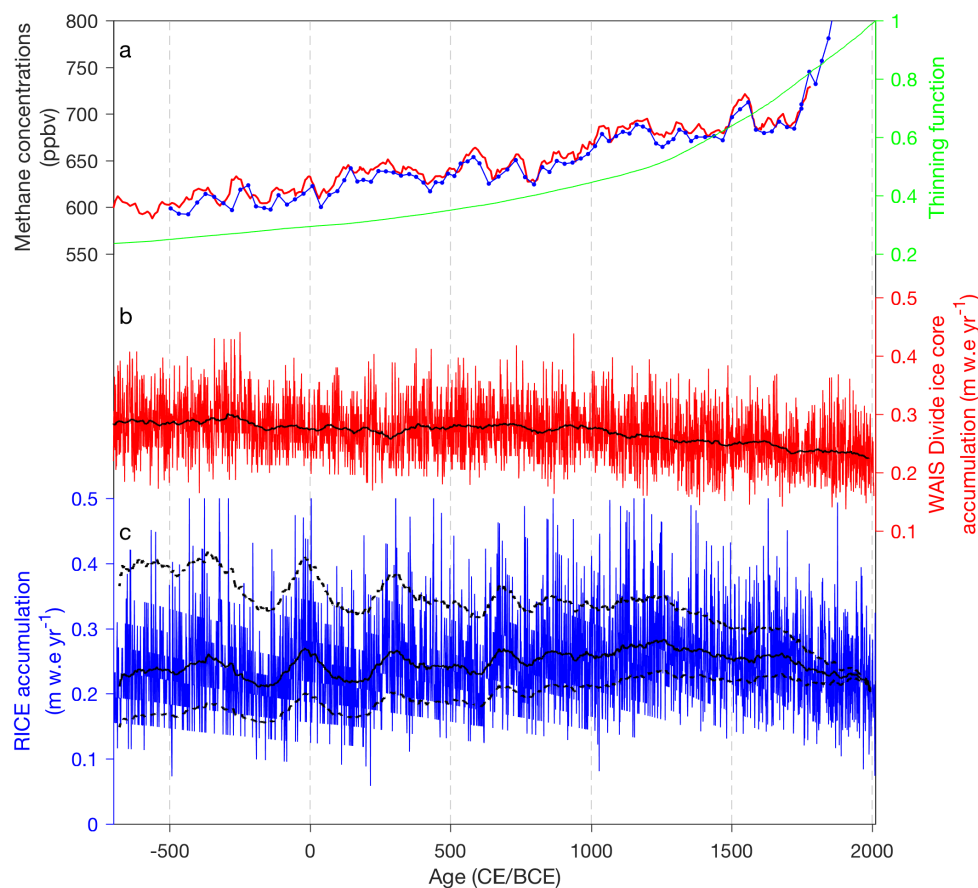
8

9

10

11

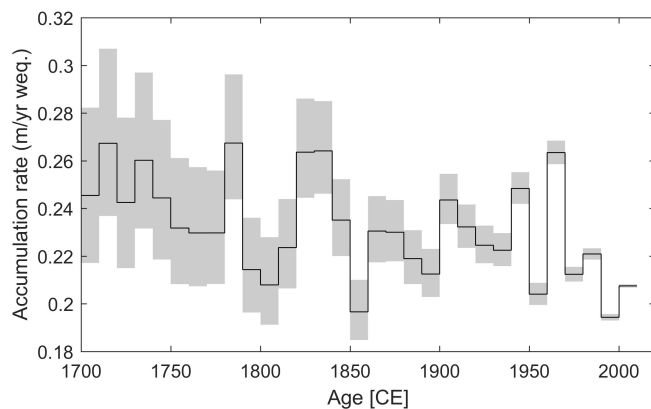
Figure 8: a) Vertical velocity measurements from pRES (Kingslake et al., 2014) and the associated fitted functions. Fit used here improves overall misfit and does not have a bias at mid-depth. b) Radar echogram with traced layers (red) and location of maximum amplitudes of the stack of Raymond arches (blue circles). The location of the modern ice divide is marked by the returns from a pole to the right (west) of the maximum bump amplitudes at depth.



1

2 **Figure 9:** **a)** Measured methane concentrations from RICE (red, on the RICE17 timescale)
3 and from WAIS Divide (blue, on the WD2014 timescale). The derived thinning function
4 (green) for the RICE core is also displayed. **b)** WAIS Divide (red) and **c)** RICE (blue)
5 accumulation histories over the past 2700 years. A 100-year smoothed version is shown in
6 black. For the RICE accumulation history, the 95% confidence interval of the derived
7 accumulation rates is shown as dotted black lines.

8



1
2
3
4
5
6

Figure 10: Decadal accumulation rates at Roosevelt Island since 1700 CE. Grey shadows indicate the 95% uncertainty bounds due to uncertainties in the thinning function.



1 **Tables**

2

3

Ice core	RID-75	RICE	RICE-12/13-B
Drilled	1974/75	2011/12 (0-130 m) 2012/13 (130-764.6 m)	Jan 2013
Depth	0-10.68 m	8.57-764.60 m	0-19.41 m
Location	79°22' S, 161°40' W	79°21.840' S, 161°42.360' W	79°21.726' S, 161°42.000' W
Analysed	1977-78	2011-13	2013
β-activity	16 cm resolution, Clausen et al. (1979)	-	-
δ¹⁸O, δD	Only δ ¹⁸ O. 4 cm resolution, Clausen et al. (1979)	Continuous and 2 cm resolution, Bertler et al. (2017)	Continuous and 2 cm resolution, Bertler et al. (2017)
CFA	-	H ⁺ , Ca ²⁺ , conductivity, dust, BC (8.57-344 m; continuous, this paper)	H ⁺ , Ca ²⁺ , conductivity, dust, BC (continuous; this paper)
ECM	-	(49-344 m; continuous, this paper)	-
IC	-	Na ⁺ , Ca ²⁺ , Mg ²⁺ , SO ₄ ²⁻ (8.57-20.6 m; 4 cm resolution, unpublished).	Na ⁺ , Ca ²⁺ , Mg ²⁺ , SO ₄ ²⁻ (4.5 cm resolution, unpublished)
ICP-MS	-	S, Na, I, Pu ²³⁹ (8.57-40 m; 2.5 cm resolution, unpublished).	S, Na, I (9.5 cm resolution, unpublished)
CH₄ δ¹⁸O_{atm}	-	discrete samples; Lee et al. (2017)	-

4

5 **Table 1:** The Roosevelt Island ice and firn core records used in this study.

6



1

Depth (m)	RICE17 age (CE)	Age confidence interval (95%)	Event	WD2014 age (CE)
0*	2013.0	[2013, 2013]	Snow surface (January 2013)	-
8.81*?	1991.6	[1990.6, 1992.6]	Eruption: Pinatubo (Philippines, May 1991)	1991.7 (1991.5-1993.5 ²)
14.62	1975.1	[1974.1, 1976.1]	Isotope match to RID-75 snow surface (winter 74/75)	-
16.19	1970.9	[1969.9, 1971.9]	Radioactivity peak (previously-determined age ¹ : winter 1970/71)	-
18.10-18.20	1965.2-1965	[1964.0, 1966.2]	Tephra: Raoul Island (New Zealand, Nov 1964)	WD ages
19.16?	1963.0	[1962.0, 1964.0]	Eruption: Agung (Indonesia, Feb 1963)?	1965.0 (1963.6-1965.6 ²)
21.98	1954.7	[1953.7, 1955.7]	Onset of high radioactivity levels: Castle Bravo, Marshall Islands (March 1954)	-
37.45	1903.8	[1902.8, 1904.8]	Eruption: Santa Maria, Guatemala (Oct 1902)	1903.6 (1902.9-1904.3 ²)
42.50	1884.5	[1883.5, 1886.0]	Eruption: Krakatau (Indonesia, Aug 1883)	1885.0 (1884.0-1886.4 ²)
47.90	1863.3	[1860.3, 1865.3]	Eruption: Makian (Indonesia, Sept. 1860/ 61)	1863.9 (1862.6-1864.6 ²)
59.38 [#]	1817.4	[1812.4, 1821.4]	Eruption: Tambora (Indonesia, April 1815)	1816.4 (1815.4-1818.4 ²)
69.63	1770.2	[1764.1, 1775.1]	Unknown	-
80.08 [#]	1722.4	[1715.3, 1728.3]	Unknown, also found in WAIS Divide, but not previously reported.	1724.0
82.47	1711.4	[1704.4, 1717.4]	Unknown	-
83.78	1705.2	[1698.2, 1711.2]	Unknown	-
84.95	1699.1	[1692.1, 1706.0]	Unknown	-
85.96	1695.1	[1687.1, 1701.1]	Unknown, also found in WAIS Divide	1696.0 (1694.6-1697.4 ²)
88.87	1680.3	[1673.2, 1687.2]	Unknown	-
97.13	1641.2	[1634.2, 1649.2]	Eruption: Parker Peak (Philippines)	1642.3 (1641.6-1643.7 ²)
101.04	1624.0	[1615.0, 1632.0]	Unknown	-
103.80	1609.2	[1600.1, 1617.1]	Unknown	-



105.58 [#]	1599.3	[1590.5, 1607.3]	Eruption: Huaynaputina (Peru)	1600.9 (1600.4-1603.3 ²)
106.56 [#]	1594.3	[1594.2, 1585.2]	Eruption: Ruiz (Columbia)?	(1594.7-1597.5 ²)
107.39 [#]	1589.9	[1580.9, 1598.9]	Unknown, also found in WAIS Divide	(1590.8-1592.3 ²)?
108.01	1587.3	[1578.3, 1595.3]	Eruption: Colima (Mexico)?	(1585.8-1587.0 ²)
110.86	1571.6	[1561.6, 1579.6]	Unknown	-
111.75	1567.3	557.3, 1575.3]	Unknown	-
113.47	1558.6	[1548.6, 1566.6]	Unknown	-
114.05	1555.2	[1545.2, 1564.0]	Unknown	-
114.19	1554.4	[1544.4, 1563.4]	Unknown	-
115.82	1546.3	[1536.3, 1554.3]	Unknown	-
115.99	1545.4	[1535.4, 1553.4]	Unknown	-
116.25	1543.4	[1533.4, 1552.4]	Unknown	-
119.59	1524.1	[1514.1, 1533.1]	Unknown	-
120.16	1520.5	[1510.5, 1530.1]	Unknown	-
120.83	1516.2	[1507.2, 1526.2]	Unknown	-
121.15	1514.3	[1505.3, 1524.3]	Unknown	-
121.85	1511.1	[1502.1, 1521.1]	Unknown	-
122.67	1507.0	[1497.0, 1517.0]	Unknown, also found in WAIS Divide	(1504.9-1508.1 ²)
123.80	1500.2	[1491.2, 1511.2]	Unknown	-
124.22	1498.1	[1489.1, 1508.1]	Unknown	-
124.91	1495.0	[1485.0, 1505.0]	Unknown	-
131.24	1457.2	[1447.2, 1468.2]	Eruption: "Kuwae" (Vanuatu)	1459.8 (1458.4-1461.4 ²)
132.02	1453.6	[1442.6, 1464.6]	Unknown, also found in WAIS Divide	(1453.4-1454.9 ²)
134.11	1441.1	[1430.1, 1451.1]	Unknown	-
145.11	1376.4	[1365.4, 1387.4]	Unknown, also found in WAIS Divide	1378.8 (1377.8-1379.7 ²)
145.93	1372.3]1361.3, 1383.7]	Unknown	-
149.57	1350.3	[1338.3, 1362.0]	Unknown	-
150.53	1345.2	[1333.2, 1356.2]	Unknown, also found in WAIS Divide	1346 (1344.5-1348.1 ²)
151.69	1337.1	[1326.1, 1349.1]	Unknown, also found in WAIS Divide	(1336.3-1337.6 ²)
152.81	1329.9	[1318.9, 1341.9]	Unknown	-
153.19	1327.5	[1316.5, 1339.5]	Unknown	-



153.68	1324.5	[1313.5, 1336.5]	Unknown	-
154.72	1316.9	[1305.9, 1329.9]	Unknown	-
155.48	1311.6	[1300.6, 1324.6]	Unknown	-
157.13	1302.0	[1290.0, 1315.0]	Unknown	-
157.61	1299.0	[1287.0, 1312.0]	Unknown	-
158.15	1295.7	[1283.7, 1308.7]	Unknown	-
159.52	1287.2	[1274.5, 1299.5]	Unknown, also found in WAIS Divide	(1285.6-1288.2 ²)
160.77	1279.2	[1266.2, 1291.2]	Unknown	-
161.01	1277.5	[1264.5, 1289.5]	Unknown, also found in WAIS Divide	(1276.5-1278.7 ²)
162.17	1269.9	[1257.0, 1282.9]	Unknown, also found in WAIS Divide	(1269.5-1271.4 ²)
164.05	1257.4	[1245.4, 1270.4]	Eruption: Samalas (Indonesia)	(1257.9-1261.1 ²)
165.04	1251.4	[1239.4, 1264.4]	Tephra: Eruption: Pleiades (West Antarctica)	1252 ± 2
166.71	1242.1	[1229.1, 1255.1]	Unknown, also found in WAIS Divide	1242.0±2.0
168.32	1231.4	[1218.4, 1245.4]	Unknown, also found in WAIS Divide	1231.0±2.0
169.60	1223.1	[1210.1, 1237.1]	Unknown	-
172.94	1201.4	[1188.4, 1217.4]	Unknown	-
173.91	1194.6	[1180.6, 1210.6]	Unknown	-
174.95	1188.0	[1174.0, 1204.9]	Unknown	-
175.56	1184.2	[1170.2, 1201.2]	Unknown	-
175.99	1181.2	[1166.2, 1198.2]	Unknown	-
176.76	1175.5	[1160.5, 1192.5]	Unknown, also found in WAIS Divide	1173±2
177.84	1166.8	[1151.8, 1183.8]	Unknown	-
178.74	1160.2	[1145.2, 1178.2]	Unknown	-
182.69	1133.0	[1116.0, 1150.0]	Unknown	-
183.35	1129.3	[1112.3, 1146.3]	Unknown	-
184.10	1123.9	[1106.9, 1140.9]	Unknown	-
184.36	1122.7	[1105.7, 1139.7]	Unknown	-
185.01	1117.7	[1100.7, 1134.7]	Unknown, also found in WAIS Divide	1111±2
185.51	1114.3	[1097.3, 1131.3]	Unknown	-
185.93	1111.2	[1094.2, 1128.2]	Unknown	-



186.44	1107.7	[1090.7, 1124.7]	Unknown	-
189.41	1086.5	[1068.5, 1104.0]	Unknown	-
195.23	1039.4	[1021.4, 1058.4]	Unknown, also found in WAIS Divide	1041±2
201.13	995.6	[975.6, 1014.6]	Unknown	-
203.47	974.3	[954.6, 993.6]	Unknown	-
204.47	966.0	[946.0, 986.0]	Unknown	-
206.03	954.1	[934.1, 974.1]	Unknown, also found in WAIS Divide	961±2
208.14	937.0	[917.0, 957.0]	Unknown	-
209.82	923.4	[903.4, 943.4]	Unknown	-
213.50	891.3	[871.3, 912.3]	Unknown	-
215.72	874.2	[853.2, 894.4]	Unknown	-
216.45	867.5	[846.5, 888.0]	Unknown	-
222.48	817.6	[795.6, 837.6]	Unknown	-
232.10	726.1	[705.1, 749.1]	Unknown	-
232.67	720.3	[699.3, 743.3]	Unknown	-
236.93	683.1	[661.1, 706.1]	Unknown, also found in WAIS Divide	686.0±2.2
237.24	680.3	[658.3, 703.3]	Unknown, also found in WAIS Divide	683.0±2.2
239.30	663.6	[640.6, 685.6]	Unknown	-
246.94	580.8	[553.8, 607.8]	Unknown	-
247.47	575.3	[548.3, 602.3]	Unknown, also found in WAIS Divide	577.0±2.4
248.76	561.3	[534.3, 589.3]	Unknown	-
250.94	539.2	[511.2, 566.2]	Unknown, also found in WAIS Divide	542.0±2.5
252.09	527.4	[499.4, 555.4]	Unknown	-
253.81	509.1	[480.1, 537.1]	Unknown	-
254.79	498.2	[469.2, 527.2]	Unknown	-
255.62	488.8	[459.8, 517.8]	Unknown, also found in WAIS Divide	495.0±2.6
256.24	481.4	[452.4, 510.4]	Unknown, also found in WAIS Divide	489.0±2.6
257.36	469.1	[440.1, 498.1]	Unknown	-
258.65	454.2	[425.2, 483.2]	Unknown	-
260.59	434.3	[404.3, 463.3]	Unknown, also found in WAIS Divide	436.0±2.8



264.16	394.9	[363.9, 424.9]	Unknown	-
265.16	381.8	[351.5, 411.8]	Unknown	-
265.79	374.2	[343.2, 404.2]	Unknown, also found in WAIS Divide	380.0±2.9
267.00	360.8	[329.8, 390.8]	Unknown	-
267.41	357.0	[325.9, 387.0]	Unknown	-
267.61	355.3	[323.3, 358.3]	Unknown	-
268.11	348.8	[317.8, 379.0]	Unknown, also found in WAIS Divide	355.0±2.9
269.36	334.1	[304.1, 366.1]	Unknown	-
269.50	332.6	[302.6, 364.6]	Unknown	-
269.93	328.2	[298.2, 360.2]	Unknown	-
270.49	322.3	[291.3, 354.3]	Unknown	-
271.08	316.4	[285.4, 347.4]	Unknown	-
272.25	305.4	[274.4, 337.4]	Unknown, also found in WAIS Divide	305.0±3.1
272.75	299.8	[268.8, 331.6]	Unknown	-
276.05	264.4	[232.4, 295.4]	Unknown, also found in WAIS Divide	267.0±3.1
279.31	224.4	[192.4, 256.4]		
280.81	205.5	[172.5, 237.5]	Unknown, also found in WAIS Divide	207.0±3.3
281.08	202.2	[169.2, 234.2]	Unknown	-
282.43	184.1	[149.1, 217.1]	Unknown	-
282.67	180.3	[145.3, 213.3]	Unknown	-
283.34	171.2	[136.2, 204.2]	Unknown, also found in WAIS Divide	171.0±3.4
283.65	166.3	[131.3, 200.3]	Unknown	-
284.79	150.4	[115.4, 184.4]	Unknown	-
284.98	148.1	[113.1, 182.1]	Unknown, also found in WAIS Divide	144.0±3.4
286.17	131.9	[96.9, 166.9]	Unknown, also found in WAIS Divide	126.0±3.5
286.40	128.3	[93.3, 163.3]	Unknown, also found in WAIS Divide	122.0±3.5
287.51	113.3	[77.3, 148.3]	Unknown	-
288.35	102.3	[66.3, 137.3]	Unknown, also found in WAIS Divide	96.0±3.5
289.18	90.9	[54.9, 126.9]	Unknown, also found in WAIS Divide	84.0±3.6



291.11	64.3	[27.3, 100.3]	Unknown	-
292.83	40.9	[3.9, 77.9]	Unknown, also found in WAIS Divide	32.0±3.7
294.27	22.9	[-14.1, 59.9]	Unknown	-
294.68	18.7	[-18.3, 55.7]	Unknown	-
294.95	15.8	[-21.2, 52.8]	Unknown	-
295.46	10.3	[-26.7, 47.3]	Unknown	-
296.12	3.1	[-33.8, 41.1]	Unknown	-
296.41	-1.6	[-37.6, 36.4]	Unknown	-
298.15	-22.0	[-59.0, 16.0]	Unknown	-
298.39	-24.3	[-61.3, 13.7]	Unknown	-
298.76	-28.0	[-65.0, 10.0]	Unknown, also found in WAIS Divide	-46.0±3.9
299.64	-38.9	[-75.9, -0.9]	Unknown	-
300.25	-47.6	[-84.6, -8.6]	Unknown	-
300.71	-52.7	[-89.7, -13.7]	Unknown, also found in WAIS Divide	-72.0±3.9
301.83	-65.8	[-104.8, -27.8]	Unknown	-
302.75	-77.8	[-117.8, -40.8]	Unknown	-
303.01	-80.9	[-120.9, -43.9]	Unknown, also found in WAIS Divide	-99.0±4.0
303.80	-94.2	[-133.2, -56.2]	Unknown	-
304.13	-97.9	[-137.9, -59.9]	Unknown	-
305.09	-112.1	[-151.1, -73.1]	Unknown	-
305.98	-125.8	[-164.8, -86.8]	Unknown, also found in WAIS Divide	-138.0±4.1
306.41	-131.0	[-171.0, -92.0]	Unknown, also found in WAIS Divide	-143.0±4.1
306.81	-136.7	[-175.7, -97.7]	Unknown	-
306.89	-138.0	[-177.0, -99.0]	Unknown, also found in WAIS Divide	-148.0±4.1
308.30	-161.0	[-201.0, -122.0]	Unknown, also found in WAIS Divide	-171.0±4.1
309.13	-174.0	[-214.0, -135.0]	Unknown	-
310.08	-188.7	[-228.7, -148.7]	Unknown	-
310.21	-190.8	[-230.8, -150.8]	Unknown	-
310.89	-202.9	[-242.8, -162.8]	Unknown, also found in WAIS Divide	-211.0±4.2
311.92	-216.8	[-257.8, -177.8]	Unknown, also found in WAIS Divide	-227.0±4.3



313.40	-239.0	[-280.0, -199.0]	Unknown, also found in WAIS Divide	-247.0±4.3
314.02	-247.7	[-288.7, -207.7]	Unknown	-
314.39	-252.6	[-293.6, -212.6]	Unknown	-
317.31	-296.1	[-338.1, -255.1]	Unknown	-
318.9	-318.8	[-359.8, -276.8]	Unknown, also found in WAIS Divide	-325.0±4.5
320.24	-334.1	[-376.1, -293.1]	Unknown, also found in WAIS Divide	-345.0±4.5
320.88	-344.6	[-385.6, -302.6]	Unknown, also found in WAIS Divide	-356.0±4.6
322.15	-362.7	[-403.7, -320.7]	Unknown, also found in WAIS Divide	-376.0±4.6
322.80	-372.1	[-413.1, -330.1]	Unknown	-
323.14	-376.7	[-417.7, -333.7]	Unknown, also found in WAIS Divide	-392.0±4.6
325.25	-405.5	[-447.5, -363.5]	Unknown, also found in WAIS Divide	-426.0±4.7
327.09	-430.7	[-472.7, -388.7]	Unknown	-
327.98	-445.2	[-487.2, -403.2]	Unknown, also found in WAIS Divide	-469.0±4.8
328.58	-456.1	[-498.1, -413.1]	Unknown	-
329.53	-469.1	[-511.1, -426.1]	Unknown	-
330.49	-484.0	[-526.0, -441.0]	Unknown	-
330.64	-486.4	[-528.4, -442.4]	Unknown	-
331.04	-491.8	[-534.8, -448.8]	Unknown	-
331.15	-495.1	[-538.1, -452.1]	Unknown, also found in WAIS Divide	-519.0±4.9
332.14	-510.9	[-553.9, -467.9]	Unknown	-
332.78	-522.5	[-565.5, -479.5]	Unknown	-
334.93	-554.6	[-598.6, -511.6]	Unknown, also found in WAIS Divide	-580.0±5.2
335.85	-567.5	[-611.5, -524.5]	Unknown, also found in WAIS Divide	-596.0±5.3
340.90	-651.0	[-695.0, -607.0]	Unknown	-
342.34	-673.3	[-719.3, -630.3]	Unknown	-
342.75	-682.1	[-727.1, -638.1]	Unknown	-
343.3	-691.4	[-745.0, -656.0]	Unknown, also found in WAIS Divide	-722.0±6.0

1 *: Depth in RICE-12/13-B shallow core. 1: Age from Clausen et al. 1979. #: CFA acidity record is missing for
 2 relevant interval, depth attribution is based on ECM and cond-Ca-relation. 2: Age interval for volcanic influx at



1 WAIS Divide from (Sigl et al. 2013), below 1258CE updated according to the new WAIS Divide timescale,
2 WD2014 (M. Sigl et al. 2016). Below 42.3m: decimal ages have been calculated assuming BC to peak Jan 1st.

3 **Table 2:** Volcanic marker horizons used for development and validation of the RICE17
4 chronology. Strata in bold were used for constraining the timescale. Synchronization to WAIS
5 Divide provides volcanic ages according to WD2014 (Sigl et al. 2015; Sigl et al. 2016). Age
6 of sulfur peak and age interval for enhanced sulfur influx is provided. RICE depths
7 correspond to volcanic peaks. Historical eruption ages (in column 4) are start date of the
8 eruptions. Unless otherwise mentioned, volcanic attribution is based on acidity, the calcium-
9 conductivity difference, ECM and/or sulfur records. Due to difficulty in RICE volcanic
10 attributions, the depth assignment corresponds to the peak values, which may occur
11 significantly later than start of the eruption. Peak values, as well as the age range for the
12 volcanic sulfur influx (Sigl et al. 2013) at the WAIS Divide site are provided.

13

14

15

16

17

Time period	Accumulation rate trend [cm w.e per century]
700 BCE – 1260 CE	+0.2 ±0.1
1260 CE – 1700 CE	-0.3 ±0.3
1700 CE – 2012 CE	-0.9 ±0.6
1950 CE – 2012 CE	-6.6 ±0.5

18

19 **Table 3:** RICE accumulation rate trends during various time periods.

20